Accepted version of the paper entitled “Plastic deformation of single crystals of the equiatomic Cr-Fe-Co-Ni medium entropy alloy – a comparison with Cr-Mn-Fe-Co-Ni and Cr-Co-Ni alloys to understand effects of Cr concentration” published in International Journal of Plasticity, vol. 169, 103732 (2023),
DOI: https://doi.org/10.1016/j.ijplas.2023.103732.

Plastic deformation of single crystals of the equiatomic Cr-Fe-Co-Ni medium entropy alloy – a comparison with Cr-Mn-Fe-Co-Ni and Cr-Co-Ni alloys

Le Li[1], Zhenghao Chen[1], Koretaka Yuge[1], Kyosuke Kishida[1], Haruyuki Inui[1], Martin Heilmaier[2], Easo P. George[3,4]

[1]Department of Materials Science and Engineering, Kyoto University, Sakyo-ku, Kyoto 606-8501, Japan
[2]Institute for Applied Materials (IAM-WK), Karlsruhe Institute of Technology (KIT), Engelbert-Arnold-Strasse 4, 76131 Karlsruhe, Germany
[3]Materials Science and Engineering Department, University of Tennessee, Knoxville, TN 37996, USA
[4]Institute for Materials, Ruhr University Bochum, 44801 Bochum, Germany

***Corresponding Author Contact Information:**
Kyosuke Kishida
Department of Materials Science and Engineering, Kyoto University,
Kyoto 606-8501, Japan
Tel: +81-75-753-5461, Fax: +81-75-753-5461,
E-mail: kishida.kyosuke.6w@kyoto-u.ac.jp

Abstract

The plastic deformation behavior of single crystals of the equiatomic Cr-Fe-Co-Ni medium-entropy alloy was investigated in compression and tension from 9 K to 1373 K. The critical resolved shear stress (CRSS) for $\{111\}\langle 1\bar{1}0\rangle$ slip is 44-45 MPa at room temperature and does not exhibit significant tension-compression asymmetry. It increases rapidly with decreasing temperature but exhibits a dulling of the temperature dependence below 77 K due to the inertia effect. The 0 K CRSS was determined to be 200 MPa by extrapolating the temperature dependence of CRSS from above 77 K to lower temperatures. This CRSS value is higher than that of the equiatomic Cr-Mn-Fe-Co-Ni high-entropy alloy, 174 MPa, but lower than that of the equiatomic Cr-Co-Ni medium-entropy alloy, 225 MPa. The rank of CRSS at 0 K of the three equiatomic alloys is consistent with the prediction of some solid solution strengthening models. The stacking fault energy (SFE) of the Cr-Fe-Co-Ni is about 20 mJ/m^2, which falls between those of the Cr-Mn-Fe-Co-Ni and Cr-Co-Ni alloys. Deformation twinning in the Cr-Fe-Co-Ni MEA occurs at a shear stress of 249 MPa on conjugate $(\bar{1}\bar{1}1)$ planes in the form of Lüders deformation at 77 K. The relationship between twinning stress and SFE is not monotonic

as previously believed, but displays a concave with a minimum twinning stress at an intermediate SFE value.

Keywords: High-entropy alloys; Single crystals; Critical resolved shear stress; Solute strengthening; Stacking fault energy; Twinning

1. Introduction

The equiatomic high-entropy alloy Cr-Mn-Fe-Co-Ni and its ternary derivative Cr-Co-Ni are known to exhibit good strength-ductility balance from ambient to cryogenic temperatures and the highest fracture toughness of all modern structural materials (Gali and George, 2013; George et al., 2019, 2020; Gludovatz et al., 2014, 2016; Gupta et al., 2022; Hua et al., 2021; Inui et al., 2022a; Li et al., 2019; Liu et al., 2022; Miracle and Senkov, 2017; Zhang et al., 2015, 2017). Studies on the Cr-Mn-Fe-Co-Ni high-entropy alloy (HEA) and its medium-entropy alloy (MEA) subsystems have revealed that solid-solution strengthening is a significant contributor to their yield strength, which can be correlated with lattice distortion (Z. Li et al., 2023; Nöhring and Curtin, 2019; Okamoto et al., 2016b; Sohn et al., 2019). Ductility can be correlated with the activation of additional deformation mechanisms including twinning and HCP (hexagonal-close packed) phase transformation (Bahramyan et al., 2020; Kim et al., 2022; Miao et al., 2017; Naeem et al., 2020; Wang et al., 2022; Wei et al., 2019; Zhang et al., 2023). Neither strength nor ductility can be correlated with the number of constituent elements in HEAs and MEAs.

Among the constituent elements, Cr in recent years has come to be recognized as being very effective in increasing both strength and ductility of HEA/MEAs (George et al., 2020; Inui et al., 2022a; Li et al., 2019). Some material parameters have been proposed to quantify the extent of solid-solution hardening of HEA and MEAs in theoretical models (Bracq et al., 2019; Inui et al., 2022b; Okamoto et al., 2016b; Toda-Caraballo, 2017; Toda-Caraballo and Rivera-Díaz-del-Castillo, 2015; Varvenne et al., 2016). Indeed, theoretical models predict the extent of solid-solution hardening of HEA and MEAs reasonably well with these materials parameters, one of which is the mean-square atomic displacement (MSAD), and all these models indicate that Cr causes severe lattice distortion compared to many other elements leading to the higher strength of Cr-Mn-Fe-Co-Ni HEAs and its MEA subsystems (Bracq et al., 2019; Inui et al., 2022b; Okamoto et al., 2016b; Varvenne et al., 2016; Wang et al., 2023; Wei et al., 2022a, 2022b).

Another possible reason for the importance of Cr as an alloying element is related to the observation that increasing the Cr content in HEAs and MEAs of the Cr-Mn-Fe-Co-Ni system decreases their SFEs (Fan et al., 2023; Hashimoto et al., 2021; Liu et al., 2018; Wagner et al., 2022; Wang et al., 2023; Zhang et al., 2020). Since the twinning shear stress decreases monotonically with decreasing SFE in FCC alloys (Christian and Mahajan, 1995; Venables, 1964), it is reasonable to expect higher Cr concentrations to facilitate deformation twinning and, in turn, enhance ductility. Therefore, it is pertinent to investigate the strength and ductility of HEAs and MEAs in the Cr-Mn-Fe-Co-Ni system as a function of Cr content to better understand the role of Cr. This has been studied in

some previous work within a single alloy system [non-equiatomic Cr-Mn-Fe-Co-Ni HEAs (Fan et al., 2023; Wagner et al., 2023) and Cr-Co-Ni MEAs (Wang et al., 2023)], in which the effects of Cr on strength and ductility are proved dominative among the constituent elements. For different equiatomic alloy systems, density functional theory calculations have indicated that those Cr-containing equiatomic HEA/MEAs usually exhibits higher MSAD and lower SFE (Huang et al., 2018; Niitsu et al., 2020; Okamoto et al., 2016; Zhao et al., 2017), but so far the direct comparison of mechanical properties experimentally obtained from bulk single crystals of different HEA/MEAs is too scarce.

In our previous studies on single crystals of the equiatomic Cr-Mn-Fe-Co-Ni HEA and the equiatomic Cr-Co-Ni MEA (Kawamura et al., 2021; Li et al., 2022), we reported that the latter had a higher critical resolved shear stress (CRSS) and ductility than the former. We ascribed these properties to the higher MSAD and lower stacking fault energy of the latter. This is consistent with what was described above about the effect of Cr concentration on mechanical properties. However, the twinning stress of the Cr-Co-Ni MEA has been reported to be higher than that of the Cr-Mn-Fe-Co-Ni HEA from experiments on polycrystals (Li et al., 2022), contrary to the long-held belief that the twinning shear stress decreases monotonically with decreasing stacking fault energy in FCC alloys. This motivated us to investigate the mechanical properties of these HEAs and MEAs with the use of single crystals with different Cr contents to deepen our understanding. The equiatomic Cr-Fe-Co-Ni MEA is a desirable candidate for this purpose, as its Cr content (25 at.% Cr) is in between those of the Cr-Mn-Fe-Co-Ni HEA (20 at.%) and the Cr-Co-Ni MEA (~33 at.%) and hence its MSAD and SFE [which govern strength and ductility (twinning stress)] are also in between those of the Cr-Mn-Fe-Co-Ni HEA and Cr-Co-Ni MEA. Previous studies on polycrystals of the equiatomic Cr-Fe-Co-Ni MEA reported that deformation twinning occurs both at 77 K and room temperature at twinning shear stresses of 208 and 239 MPa, respectively (Wang et al., 2018) and 281 MPa from 25 K to room temperature (independent of temperature) (Naeem et al., 2021). However, these values for twinning may well be affected by the grain size effect. Limited experimental results can be found for single crystal of the equiatomic Cr-Fe-Co-Ni MEA. Wu et al. reported that the CRSS for {111}<110> slip is 39-43 MPa and 96-99 MPa at room temperature and 77 K, respectively, but they did not investigate the twinning behavior at all (Wu et al., 2015).

In the present study, we investigate the plastic deformation behavior of single crystals of the equiatomic Cr-Fe-Co-Ni MEA in compression and tension from 9 K to 1373 K to deduce the temperature dependence of CRSS, twinning shear stress, tensile ductility at room temperature and 77 K, and stacking fault energy. The mechanical properties of the Cr-Fe-Co-Ni MEA are compared with those of the Cr-Mn-Fe-Co-Ni

HEA and Cr-Co-Ni MEA in Section 3. In Section 4, the thermally activated behavior of dislocations is analyzed based on the classical model for conventional FCC solid-solutions. Then, solid-solution strengthening is quantitatively calculated by several different models to understand the role of Cr. Finally, the effects of Cr on the stacking fault energy and deformation twinning stress are discussed.

2.1. Experimental Procedures

High-purity (>99.9%) elemental metals (Cr, Fe, Co, Ni) were arc melted in argon to produce rods of the equiatomic Cr-Fe-Co-Ni alloy which were then grown into single crystals using procedures similar to those described in an earlier paper (Li et al., 2022). The single crystals were annealed at 1473 K for 168 hours, followed by water quenching. After crystallographic orientations were determined by the Laue method, [$\bar{1}$23]-oriented tension and compression specimens with gauge dimensions of 2 × 2 × 5 mm^3 were cut by spark-machining and their surfaces polished mechanically and electrolytically with a solution of nitric acid and methanol (1:4 by volume). Compression and tension tests were conducted at temperatures between 9 K to 1373 K at an engineering strain rate of 1×10^{-4} s^{-1}. Strain rate change tests were performed below room temperature to measure the strain-rate sensitivity of flow stress. Deformation markings on specimen surfaces were examined in a light microscope and scanning electron microscope (SEM) equipped with an electron back-scatter diffraction (EBSD) system. Deformation fine structures were examined by transmission electron microscopy (TEM) and scanning transmission electron microscopy (STEM) with JEOL JEM-2000FX and JEM-ARM200F electron microscopes. Thin foils for TEM observations were prepared by electro-polishing with a solution of perchloric acid, n-butanol, and methanol (1:2:7 by volume).

2.2. Theoretical calculations

The optimized SQS (special quasirandom structure, Zunger et al., 1990) configurations are constructed for supercell of 600-atom (i.e., 5 × 5 × 6 expansion of FCC conventional 4-atom unit cell) based on Monte Carlo simulation to minimize Euclidean distance between correlation functions up to 4th nearest neighbor pair for practically-constructed configurations and those for ideal ones.

MSAD for SQS configurations are estimated based on density functional theory (DFT) calculation (Kresse and Furthmüller, 1996). We perform total energy calculation by VASP code using projector-augumented wave method, with the exchange–correlation functional treated under the generalized-gradient approximation of Perdew-Burke-Ernzerhof (GGA-PBE). The plane wave cutoff of 360 eV is used. Structural optimization is performed until the residual forces become less than 0.001 eV/Å, where cell-shape is kept fixed on cubic while lattice parameter and internal atomic positions are relaxed. k-

point sampling is performed on the basis of the Monkhorst-Pack scheme with gamma point as well as 2 × 2 × 2 grids for representative configurations, confirming that the former sampling condition is sufficient for the present purpose.

3. Results

3.1. Compressive deformation behavior

3.1.1. Temperature dependence of CRSS

Yielding occurs smoothly in compression without any load drop in the [$\bar{1}$23]-oriented single crystals of the equiatomic Cr-Fe-Co-Ni MEA at all temperatures (Fig. S1). Slip trace analysis, Fig. S2, confirms the operation of (111)[$\bar{1}$01] slip whose CRSS values (determined from the 0.2% offset yield stress and the corresponding Schmid factor of 0.467) are plotted in Fig. 1 as a function of temperature, together with those for the equiatomic Cr-Mn-Fe-Co-Ni HEA and Cr-Co-Ni MEA (Kawamura et al., 2021; Li et al., 2022). The temperature dependence of CRSS is qualitatively similar in the three alloys: it increases rapidly with decreasing temperature below room temperature but less so above room temperature. There is a slight increase of CRSS with increasing temperature between 873 K and 1273 K. The CRSS increases rapidly from 44-45 MPa at room temperature to 99-102 MPa at 77 K, consistent with those (39-43 MPa at room temperature and 96-99 MPa at 77 K) previously reported for single crystals of the equiatomic Cr-Fe-Co-Ni MEA by Wu et al. (Wu et al., 2015). However, here, a dulling of the temperature dependence of CRSS is observed below 77 K, unlike in Wu et al. where tests below 77 K were not performed. This dulling effect at low temperatures (typically below about 50 K) has been seen previously in dilute FCC solid-solution alloys such as Cu-Al alloys (Kawamura et al., 2021), as well as in the Cr-Co-Ni MEA (Li et al., 2022), and is believed to be due to the inertia effect (Granato, 1971; Schwarz et al., 1977). The degree of dulling [defined here as the CRSS difference at 0 K between the extrapolated curve (solid line) and dotted curve (drawn through the experimental data points), see inset of Fig 1] increases with increasing Cr content (i.e., in the order Cr-Co-Ni > Cr-Fe-Co-Ni > Cr-Mn-Fe-Co-Ni). Above 873 K, a slight increase in CRSS is observed in the Cr-Fe-Co-Ni MEA, accompanied by serrations in the stress-strain curves, Fig. S1, similar to what has been previously reported in equiatomic Cr-Mn-Fe-Co-Ni and its subsets (Kawamura et al., 2021; Li et al., 2022; Tsai et al., 2019). The increase in CRSS above 873 K is attributed to the Portevin-Le Chatelier (PLC) effect as in many FCC binary solid-solution alloys. In FCC solid-solutions, the PLC effect is considered to originate from the interaction between dislocations and solute atoms, which occurs when the deformation temperature is high enough for atomic diffusion of solute atoms to occur at a speed comparable to that of dislocations (Rodriguez, 1984; Tsai et al., 2019). Here, the increase

in CRSS increases with decreasing Cr content (i.e., in the order Cr-Mn-Fe-Co-Ni > Cr-Fe-Co-Ni > Cr-Co-Ni). We suspect Mn and Fe play a role in the occurrence of the PLC effect. However, the detailed mechanism behind the PLC effect in these alloys is not known and is the subject of ongoing research.

To deduce the CRSS at 0 K, the experimentally obtained CRSS values are fitted with the following conventional equation (Kocks et al., 1975; Wille et al., 1987; Wille and Schwink, 1986),

$$\tau(T) = \tau_{ath} + \tau_{th}\left[1-\left(\frac{T}{T_a}\right)^{\frac{1}{q}}\right]^{\frac{1}{p}} \quad (1)$$

where T_a is the athermal temperature above which the CRSS becomes temperature-independent (873 K for the Cr-Fe-Co-Ni MEA), τ_{ath} is the athermal stress, i.e. CRSS at T_a, τ_{th} is the thermal stress, and p and q are fitting parameters. We only used CRSS values obtained from above 77 K for the fitting to avoid interference from the inertia effect at lower temperatures. The fitting results are tabulated in Table 1 and the fitted curves are shown in Fig. 1. From the fitted curves, the CRSS at 0 K for the equiatomic Cr-Fe-Co-Ni MEA is 200 ± 10 MPa, which is higher than that (174 ± 6 MPa) for the Cr-Mn-Fe-Co-Ni HEA and lower than that (225 ± 7 MPa) for the Cr-Co-Ni MEA (Kawamura et al., 2021; Li et al., 2022). Thus, the CRSS at 0 K seems to increase with increasing Cr content, as expected from the magnitudes of their MSADs (which will be discussed in a later section). Interestingly, at the selected testing temperatures, the CRSS of the equiatomic Cr-Fe-Co-Ni MEA is only a bit higher (near room temperature) and even a bit lower than that of the equiatomic Cr-Mn-Fe-Co-Ni HEA, while the 0 K CRSS for the Cr-Fe-Co-Ni MEA is much larger than that of the Cr-Mn-Fe-Co-Ni HEA. This is because a crossover of the fitting curves for the temperature dependence of CRSS of the equiatomic Cr-Mn-Fe-Co-Ni HEA and Cr-Fe-Co-Ni MEA occurs at a very low temperature. As we described in Section 3.1.1 and 3.1.2, the dulling of the temperature dependence of CRSS occurs below 77 K due to the “inertia effect” in the Cr-Fe-Co-Ni MEA so that the fitting of the CRSS-temperature curves is performed only with the data points above 77 K where the CRSS values are not affected by the inertia effect. However, no such dulling of the temperature dependence of CRSS is observed, at least, until 10 K in the equiatomic and non-equiatomic quinary Cr-Mn-Fe-Co-Ni HEAs in our previous work (Kawamura, et al., 2021; Fan et al., 2023), albeit the reason is unclear yet. The fitting of the CRSS-temperature curves is thus made with all the data down to 10 K for the Cr-Mn-Fe-Co-Ni HEA. This indicates that the yield stress at finite temperatures does not represent the intrinsic alloy strength (defined at 0 K in the absence of thermal activation); that is,

thermally activated dislocation motion contributes significantly to strength at finite temperatures such as room temperature.

3.1.2. Strain-rate sensitivity of flow stress

Strain-rate sensitivity of flow stress was measured for [$\bar{1}$23]-oriented single crystals of the equiatomic Cr-Fe-Co-Ni MEA in the plastic strain range of stage I hardening at temperatures between 9 K and room temperature (Fig. S1). The results are plotted in Fig. 2(a) which show that the flow stress increases with increasing strain rate at all temperatures. When the data in Fig. 2(a) are differentiated, it shows that the strain-rate sensitivity of flow stress increases with decreasing temperature up to 77 K and then decreases rather rapidly with decreasing temperature, Fig. 2(b). The decrease observed below 77 K is clear evidence for the inertia effect (Granato, 1971; Schwarz et al., 1977), through which the dulling of the temperature dependence of CRSS occurs (Fig. 1).

3.1.3. Dislocation structures

Fig. 3(a) shows typical dislocations observed in a [$\bar{1}$23]-oriented single crystal of the Cr-Fe-Co-Ni MEA after compression to 2-3% plastic strain at room temperature. Long and smoothly curved dislocations without any preferred orientations (edge or screw) are observed in thin foils cut parallel to the (111) primary slip plane. As expected, cell structures are not observed at such low strains. The planarity of dislocation structure is indicative of low SFE. Indeed, dislocations widely dissociated into coupled Shockley partial dislocations are clearly revealed by weak-beam dark-field microscopy (Fig. 3(b)). From the dissociation widths measured here as a function of the angle (θ) between dislocation line vector and Burgers vector, and the shear modulus of this alloy (Laplanche et al., 2018), the SFE of the equiatomic Cr-Fe-Co-Ni MEA is evaluated to be 20 ± 4 mJ/m^2. Similar to our previous works on the Cr-Mn-Fe-Co-Ni HEA and Cr-Co-Ni MEA (Kawamura et al., 2021; Li et al., 2022; Okamoto et al., 2016a), the extent of scatter in dissociation widths at a given θ is neither unprecedented nor unique but is comparable to those in some pure FCC metals (Cockayne et al., 1971; Stobbs and Sworn, 1971). The reader may refer to the paper (Okamoto et al., 2016a) for some more details of the method. The deduced SFE (20 ± 4 mJ/m^2) of our Cr-Fe-Co-Ni MEA is lower than that (27 ± 4 mJ/m^2) determined previously by weak-beam dark-field microscopy in polycrystalline Cr-Fe-Co-Ni (Liu et al., 2018) and that (32.5 mJ/m^2) determined by neutron diffraction in polycrystalline Cr-Fe-Co-Ni (Wang et al., 2018). Our equiatomic Cr-Fe-Co-Ni MEA (this study) has a SFE that is in between that (30 ± 5 mJ/m^2) of the Cr-Mn-Fe-Co-Ni HEA (Kawamura et al., 2021) and that (14 ± 3 mJ/m^2) of the Cr-Co-Ni MEA (Li et al., 2022), all of which were determined using single crystals under similar experimental conditions

(weak-beam, dark field TEM). Previous work has indicated that Ni increases the SFE while Cr and Co decrease the SFE with Cr being far more effective from the analysis of SFE in various quinary Cr-Mn-Fe-Co-Ni HEAs and ternary Cr-Co-Ni MEAs (Bertoli et al., 2021; Fan et al., 2023; Wang et al., 2023; Yan et al., 2023). We therefore suspect that the decrease in SFE of the present three alloys is also due to the increase of Cr content, albeit more studies in different MEAs are still required to make a definite conclusion.

3.2 Tensile deformation behavior

3.2.1. Stress-strain curves

Tensile engineering stress-strain curves of [$\bar{1}$23]-oriented single crystals of the Cr-Fe-Co-Ni MEA at room temperature and 77 K are shown in Fig. 4(a). From these, true stress-strain curves were obtained and are shown in Fig. 4(b). At room temperature, stage I (concave-upward shape accompanied by a moderate yield drop) extends to about 20% plastic strain followed by stage II until failure occurs. The room-temperature CRSS (at yielding) is 43 MPa, which is comparable to that obtained in compression (44-45 MPa), indicating the absence of significant tension-compression asymmetry (Fig. S3), similar to what was previously reported for Cr-Mn-Fe-Co-Ni and Cr-Co-Ni (Kawamura et al., 2021; Li et al., 2022). Deformation twinning is not observed to occur at room temperature even when stretched to failure (as confirmed by EBSD/SEM (Fig. S4) and TEM observations). This is in contrast to polycrystals of the Cr-Fe-Co-Ni MEA in which room temperature twinning was reported to occur in tension at a true stress of 730 ± 30 MPa and true strain of 0.212 (Wang et al., 2018) or 860 ± 20 MPa true stress and 0.286 true strain (Naeem et al., 2021). However, in both these works on polycrystals (Naeem et al., 2021; Wang et al., 2018), the occurrence of twinning was deduced from stacking fault probability determined from neutron scattering data and not by direct observation of deformation twins.

At 77 K, the CRSS of single crystals of the Cr-Fe-Co-Ni MEA increases to 99 MPa, which is again comparable to that (99-102 MPa) obtained at 77 K in compression in the present study (Fig. S3). Stage I extends to more than 29% plastic strain with a concave upward shape and a more pronounced load drop (~24 MPa at 77 K compared to ~5 MPa at room temperature). Similar stress-strain behavior in stage I has also been observed in our previous work on [$\bar{1}$23]-oriented single crystals of the equiatomic Cr-Co-Ni MEA (L. Li et al., 2022, 2023). In one of those studies (L. Li et al., 2023), we demonstrated a lack of correlation between the magnitude of load drop and the degree of short-range ordering. Here, we find a temperature dependence of the magnitude of load drop in stage I, the explication of which needs further investigation in future studies.

In tensile stress-strain curves (Figs. 4(a) and (b)), an inflection point is clearly visible

in the 77 K curve after stage II work-hardening, accompanied by a sudden change in work hardening rate (Fig. 4(c)). Interrupted tensile tests (Fig. 5(a)) confirm the inflection point is due to the onset of deformation twinning on the $(\bar{1}\,\bar{1}\,1)$ conjugate planes (Figs. 5(b) and 5(d)) which propagates like a Lüders band from one end of the gauge section to the other. This is the same behavior as we saw previously in $[\bar{1}23]$-oriented single crystals of the Cr-Mn-Fe-Co-Ni HEA and Cr-Co-Ni MEA tested at 77 K (Kawamura et al., 2021; Li et al., 2022). The tensile loading axis at the inflection point is determined to be $[\bar{1}3,12,25]$ (Fig. 5(c)). The extent of 'overshoot' of the tensile loading axis orientation beyond the [001]-$[\bar{1}11]$ symmetry line during stage I and II straining is calculated to be 1.3°. Similar overshoots occurred in the Cr-Mn-Fe-Co-Ni HEA at 3.7° (Kawamura et al., 2021) and in the Cr-Co-Ni MEA at 4.7° (Li et al., 2022). This is inconsistent with the long-held belief in FCC alloys that the extent of the tensile loading axis 'overshoot' is related inversely to stacking fault energy.

From the inflection point in the true stress-strain curve of Fig. 4(b), the onset stress for deformation twinning at 77 K is determined to be 615 MPa. Then, with the Schmid factor (0.405) for the $(\bar{1}\,\bar{1}\,1)[\bar{1}\,21]$ conjugate twinning system at the loading axis orientation of $[\bar{1}3,12,25]$, the onset twinning shear stress is calculated to be 249 MPa. This twinning shear stress is comparable to that (274 MPa) from model prediction using the calculated unstable stacking fault energy (Huang et al., 2018) and to that (281 ± 7 MPa) experimentally determined for polycrystals of the Cr-Fe-Co-Ni MEA (axial stress divided by the Taylor factor). However, the twinning shear stress of the Cr-Fe-Co-Ni MEA (present study) is considerably lower than those of Cr-Mn-Fe-Co-Ni and Cr-Co-Ni MEA experimentally determined in our previous works with $[\bar{1}23]$-oriented single crystals at 77 K (343 and 482 MPa, respectively). This will be discussed further in section 4.2.

The plastic strains at failure, both at 77 K and room temperature, for the Cr-Fe-Co-Ni MEA is in between those for the Cr-Mn-Fe-Co-Ni HEA and the Cr-Co-Ni MEA (Kawamura et al., 2021; Li et al., 2022), so that it increases with decreasing SFE (i.e., with increasing Cr content) for these three alloys, consistent with the general trend in FCC alloys.

3.2.2. Deformation fine structures

Fig. 6(a) shows a typical dark-field TEM image of deformation twins in a $[\bar{1}23]$-oriented single crystal of the Cr-Fe-Co-Ni MEA deformed to failure at 77 K. The thin foil was cut perpendicular to the $(\bar{1}\,\bar{1}\,1)$ conjugate twinning planes and the dark-field image of Fig. 6(a) was formed by setting an objective aperture at the diffraction spot corresponding to twins (see the inset diffraction pattern). Although some thick twins (50~60 nm) can be occasionally seen, most of deformation twins are thin, around ten

nanometers in thickness, as shown in the thickness distribution histogram of Fig. 6(b). The average twin thickness (16.3 nm) of the Cr-Fe-Co-Ni MEA is again between that (20.1 nm, see Fig. S5) of the Cr-Mn-Fe-Co-Ni HEA and that (12.3 nm) of the Cr-Co-Ni MEA (Li et al., 2022) obtained similarly from dark-field TEM images. Further atomic-resolution STEM observations, Fig. 6(c), clearly reveal the existence of thin HCP layers not only associated with twins but also isolated from twins. Histograms of twin and HCP layer thickness distributions evaluated with atomic-resolution STEM images are shown in Fig. 6(d). Twin thicknesses determined from atomic-resolution STEM images tend to give smaller values when compared to those from dark-field TEM images, as thin matrix layers (M) and thin stacking faults embedded in a twin (SF) can also be visible. But the overall tendency is the same regardless of whether dark-field TEM images or atomic-resolution STEM images are used as the source for measurement. The average twin thickness (5.2 nm) of twins in the Cr-Fe-Co-Ni MEA is in between those of the Cr-Co-Ni MEA (Li et al., 2022) and Cr-Mn-Fe-Co-Ni HEA. Thus the twin thickness increases with increasing SFE, as has long been believed to be the case in FCC alloys (Christian and Mahajan, 1995; Venables, 1964). Atomic-resolution STEM imaging also reveals, however, that the average thickness (1.0 nm) of HCP layers in the Cr-Fe-Co-Ni MEA is smaller than the 2.1 nm thick layers in the Cr-Co-Ni MEA (Li et al., 2022) and that such HCP layers are rarely resolved in the Cr-Mn-Fe-Co-Ni HEA (Kawamura et al., 2021). In contrast to the behavior of deformation twins, it appears that HCP layers become thicker with decreasing stacking fault energy. This may be related to the stability of the HCP phase with respect to the FCC phase.

4. Discussion

4.1. Thermally activated glide of dislocations

The activation volume (V) for plastic deformation can be estimated from the strain rate ($\dot{\gamma}$) sensitivity of flow stress (τ) (Fig. 2) and the following conventional equation (Butt and Feltham, 1978; Conrad, 1964),

$$V = kT\left[\frac{\partial \ln \dot{\gamma}}{\partial \tau}\right]_T \tag{2}$$

where k is the Boltzmann constant, T is the absolute temperature. The calculated activation volume of the Cr-Fe-Co-Ni MEA is plotted in Fig. 7(a) as a function of temperature, together with those of the Cr-Mn-Fe-Co-Ni HEA (Kawamura et al., 2021) and Cr-Co-Ni MEA (Li et al., 2022) for comparison. All three activation volumes decrease with decreasing temperature. Above 77 K, the Cr-Co-Ni MEA exhibits the lowest value of activation volume, followed by Cr-Fe-Co-Ni and Cr-Mn-Fe-Co-Ni in

decreasing order of Cr content. The particular interest of Cr arises from the fact that although the Co and Ni contents also decrease in the three alloys, the MSAD (also misfit volume and size misfit) of Cr is significantly larger than that of Co and Ni (Okamoto et al., 2016b; Toda-Caraballo, 2017; Varvenne et al., 2016). Below 77 K, where dislocation motion can be influenced by the inertia effect, the Cr-Co-Ni MEA exhibits the highest value of activation volume, followed by Cr-Fe-Co-Ni MEA and Cr-Mn-Fe-Co-Ni HEA in decreasing order of Cr content. This order is opposite to that above 77 K, but is consistent with the order of the dulling of temperature dependence of CRSS (Fig. 1), confirming that the latter is due to the inertia effect.

According to Butt et al. (Butt and Feltham, 1993; Butt, 1998), the temperature dependence of activation volume of FCC solid solutions can be expressed with the following equation,

$$V = V_0 \exp(\frac{-mkT}{W_0}) \quad (3)$$

where V_0 is the activation volume at 0 K, m is a constant around 27 and W_0 is a material-dependent constant. We fitted the deduced activation volumes above 77 K (to avoid the inertia effect) to equation (3), and the results are shown in Fig. 7(b) and Table 1. The activation volume at 0 K (V_0) is the intercept with the vertical axis of Fig. 7(b). Not only does this activation volume decrease with increasing Cr content in the three alloys, but the activation volume at all temperatures below room temperature also decreases with increasing Cr content, Fig. 7(c). This is consistent with the general view that the activation volume is inversely correlated with the significance of the temperature dependence of CRSS in FCC solid solution alloys. The fact that the activation volume increases with increasing Cr content suggests that Cr is important in hindering dislocation motion in these solid solution alloys.

The activation enthalpy (U) for deformation can be estimated with the following conventional equation (Li et al., 2022; Suzuki and Kuramoto, 1968),

$$U = -k \frac{\ln \dot{\gamma}(\tau, T_2) - \ln \dot{\gamma}(\tau, T_1)}{\frac{1}{T_2} - \frac{1}{T_1}} \quad (4)$$

where T_1 and T_2 are two different absolute temperatures for deformation. We calculated the activation enthalpy for deformation in Fig. 7(d) as a function of shear stress from the strain rate ($\dot{\gamma}$) sensitivity of flow stress (τ) (Fig. 2) for the alloys being considered here. All three alloys have activation enthalpies of around 0.6-0.7 eV at shear stress levels corresponding to the room-temperature values (when tested at a strain rate of 1×10^{-4} s^{-1}). These activation enthalpies are similar to those of conventional FCC alloys at room temperature (Suzuki and Kuramoto, 1968). This is consistent with the proposal by

Basinski et al. that a single mechanism governs the thermally activated motion of dislocations in FCC solid solution alloys (Basinski et al., 1972).

Basinski et al. proposed the concept of 'stress-equivalence' according to which both the temperature and strain-rate dependence of CRSS correlate with the magnitude of solid-solution hardening rather than the type of solute or its concentration (Basinski et al., 1972). Their work revealed that (i) the yield strength at 77 K (σ_{77K}) is proportional to the difference between the yield strength at 77 K and room temperature (σ_{298K}) and (ii) the activation volumes at 77 K and room temperature fall on their respective master curves when plotted as a function of yield stress. We have confirmed that the concept of 'stress-equivalence' holds true also for the three HEA/MEAs, as shown in Figs. 8(a) and (b), respectively. This clearly indicates that all the three HEA/MEAs are strengthened by a solid-solution hardening mechanism.

4.2. CRSS at 0 K for FCC HEAs and MEAs

The main strengthening mechanism for the present Cr-Fe-Co-Ni MEA and also for the Cr-Mn-Fe-Co-Ni HEA and Cr-Co-Ni MEA is solid-slution hardening, as discussed above. We evaluate solid-solution hardening in these HEA/MEAs with the help of some recent models proposed for solid-solution hardening in HEAs and MEAs. Toda-Caraballo et al. proposed a model based on Gypen's work in multicompont systems that was extened from Labusch's theory (Gypen and Deruyttere, 1977a, 1977b; Labusch, 1970; Toda-Caraballo and Rivera-Díaz-del-Castillo, 2015), in which solid-solution hardening arises from the interaction between dislocations and solutes through atomic size misfit (δ_n) and shear modulus misfit (η'_n) of the solute *n*, as described by the following equations,

$$\delta_n = \frac{\partial a}{\partial c_n}\frac{1}{a} \text{ and } \eta'_n = \frac{\eta_n}{1+0.5|\eta_n|} \text{ with } \eta_n = \frac{\partial \mu}{\partial c_n}\frac{1}{\mu} \quad (5)$$

where a is the lattice parameter, and μ is the shear modulus. The CRSS at 0 K is then calculated to be

$$\tau_0 = \left[\sum\nolimits_n B_n^{3/2} c_n\right]^{2/3} \text{ with } B_n = \mu\left(\eta'^2_n + \alpha^2\delta_n^2\right)^{2/3} Z \quad (6)$$

where Z is a fitting constant and α is a parameter accounting for the difference in interaction energy between screw/edge dislocations and solutes. Here, α = 16 is adopted for the edge-dislocation/solutes interaction following earlier work (Jax et al., 1970). Fig. 9(a) shows the results of our estimation for the two different contributions, atomic size misfit and shear modulus misfit, to solid-solution hardening. In the present HEA/MEAs, the atomic size misfit term (rather than the shear modulus misfit term) is found to make a major contribution to solid-solution hardening with its contribution increasing with increasing Cr content. Using the previously determined value of the fitting parameter Z = 3.030 for equiatomic Cr-Mn-Fe-Co-Ni HEA (Fan et al., 2023), we

calculated the 0 K CRSS for Cr-Fe-Co-Ni and Cr-Co-Ni and compared them to the experimentally determined CRSS values, Fig. 9(b). The 0 K CRSS values predicted by the Toda-Caraballo model are in reasonable agreement with experimental values. However, it must be noted that so far no clear physical meaning has been given to the Z parameter and its value varies all over the place from $Z = 3.030$ here, to 5 in Toda-Caraballo et al. (Coury et al., 2018; Toda-Caraballo, 2017) for solid-solution alloys of the Cr-Co-Ni system to 1.9, 1.4 and 0.8 for dilute Ag, Au and Cu binary FCC solid-solution alloys, respectively (Jax et al., 1970).

Another parameter, the mean-square atomic displacement (MSAD), which is a measure of the average displacements of the constituent elements from the ideal FCC lattice positions, has been shown to correlate with the 0 K CRSS of FCC HEAs and MEAs (Fan et al., 2023; Inui et al., 2022b; Okamoto et al., 2016b). Fig. 10(a) shows the MSAD values for each of the constituent elements and their averaged values for the three HEA/MEAs of interest here. A notable feature is that Cr exhibits the highest MSAD value in all three alloys. As expected from the 'intermediate' Cr concentration in the Cr-Fe-Co-Ni MEA, the average MSAD value of this alloy lies between those of the Cr-Mn-Fe-Co-Ni MEA and the Cr-Co-Ni MEA. This agrees well with our previous work that the contribution to MSAD ranks as Cr>Mn>Fe>Co>Ni within the quinary Cr-Mn-Fe-Co-Ni alloy system, and both the MSAD of Cr and the averaged MSAD increase with increasing Cr concentration (Fan et al., 2023). This is also consistent with the results in Fig. 9(a) that Cr plays an important role in strengthening these HEA/MEAs. We therefore plotted the 0 K CRSS normalized by shear modulus μ as a function of the square root of the averaged MSAD normalized by the magnitude of Burges vector in Fig. 10(b). The 0 K shear moduli were obtained by extrapolating the experimental temperature-dependent shear moduli reported by Laplanche et al. (Laplanche et al., 2015, 2018). A good linear relationship is observed, indicating that MSAD is a reasonable scaling factor to predict solid-solution hardening in FCC HEA/MEAs. Additional work on single crystals of other equiatomic quaternary and ternary MEAs is needed to establish the broader validity of this linear correlation.

4.3. Deformation twinning

4.3.1. Relation between twinning stress and stacking fault energy

Since the review article by Venables (Venables, 1964), it is generally believed that the twinning shear stress (τ_{twin}) increases with increasing SFE in FCC alloys. An example of this is shown at the bottom of Fig. 11(a) for Cu-base binaries. Recently, however, Szczerba et al. reported the opposite trend for single crystals of binary Cu-Al solid-solution alloys (Szczerba and Szczerba, 2017). The opposite trend was also reported for

polycrystals of Cr-Mn-Fe-Co-Ni, Cr-Fe-Co-Ni and Cr-Co-Ni (open symbols, top of Fig. 11(a)) (Laplanche et al., 2016, 2017; Naeem et al., 2021), although there is some uncertainty in these results arising from grain size effects on the twinning stress. Confounding effects of grain size can be avoided by considering [$\bar{1}$23]-oriented single crystals and, in that case, the twinning shear stress of the Cr-Fe-Co-Ni MEA (present study) is considerably lower than those of the Cr-Mn-Fe-Co-Ni HEA and the Cr-Co-Ni MEA (Kawamura et al., 2021; Li et al., 2022), all determined at 77 K (solid symbols, top of Fig. 11(a)). As shown in Fig. S6(a), the SFE (right Y axis) decreases monotonically with the Cr concentration whereas a concave upward correlation is observed between the twinning shear stress (left Y axis) and Cr concentration with the Cr-Fe-Co-Ni MEA of 0.25 Cr (atomic fraction) showing the minimum value for twinning stress. This unexpected result clearly indicates that the twinning shear stress does not vary monotonically with stacking fault energy, contrary to previous reports of binary FCC solid-solution alloys (Christian and Mahajan, 1995; Venables, 1964) and polycrystals of these FCC HEA/MEAs (Laplanche et al., 2017, 2016; Naeem et al., 2021).

Szczerba et al. (Szczerba and Szczerba, 2017) proposed the following equation to account for the decreasing twinning stress with increasing SFE in single crystals of binary Cu-Al solid-solution alloys,

$$\tau_{\text{twin}} = \tau_{\text{s}} + \frac{\gamma_{\text{isf}}}{b_{\text{twin}}} + \tau_{\text{D}} \qquad \text{with} \qquad \tau_{\text{D}} \propto \frac{1}{\gamma_{\text{isf}}} \tag{7}$$

where τ_{s} is the CRSS for slip, γ_{isf} is the intrinsic stacking fault energy, b_{twin} is the magnitude of the Burgers vector of the twinning dislocation, and τ_{D} is the interaction stress between twinning dislocation and forest dislocations (Wessels and Nabarro, 1971). This equation implies that for deformation twinning to occur at τ_{twin}, three barriers must be overcome: the stress barrier for slip (first term), the stress barrier to nucleate a twinning partial dislocation (second term), and the stress barrier to propagate a twinning partial dislocation through forest dislocations (third term). It has been proposed that the third term (τ_{D}) is inversely proportional to the stacking fault energy (Wessels and Nabarro, 1971). Equation (7) predicts that the twinning shear stress first decreases and then increases with increasing stacking fault energy.

When the twinning stress at 77 K is considered in light of equation (7), the first term corresponds to the CRSS at 77 K, while the second term can be calculated from the stacking fault energy and the lattice constant. By subtracting the sum of the first and second terms from the experimentally determined twinning stress, the third term can be deduced. These three terms are plotted in Fig. 11(b) as a function of stacking fault energy for the three HEA/MEAs (SFE decreases with increasing Cr content and is 30, 20 and 14 mJ/m^2 for the quinary, quaternary, and ternary alloys, respectively). These three terms are

also plotted in Fig. S6(b) as a function of Cr concentration to clearly indicate its effects. The variation of the first term is too small to account for the concave-upward variation of twinning stress with stacking fault energy seen Fig. 11(a). The second term increases with increasing stacking fault energy (with decreasing Cr content (Fig. S6(b)), suggesting a higher contribution at higher stacking fault energies (at lower Cr contents). The third term decreases rather rapidly with increasing stacking fault energy (with decreasing Cr content). This is consistent with what is proposed by Szczerba et al. (Szczerba and Szczerba, 2017) (τ_D inversely proportional to the stacking fault energy) and suggests a higher contribution at lower stacking fault energies. The above analysis clearly indicates that the decrease in twinning stress at lower stacking fault energies is due to the contribution from the third term corresponding to the stress barrier for twinning dislocations to propagate through the extended forest dislocations.

Obviously, the long-held belief that the twinning stress increases with increasing stacking fault energy relies solely on the contribution of the second term of equation (7) that involves only the intrinsic stacking fault energy (γ_{isf}) and the magnitude of the Burgers vector of the twinning dislocation (b_{twin}). However, experimentally determined twinning stresses with single crystals are known to vary (sometimes very significantly) with the initial loading axis orientation so that plastic strain levels at the onset of deformation twinning differ considerably even for the same material. This can also occur if the stacking fault energy changes. Indeed, the plastic true strain at the onset of deformation twinning decreases significantly from ~0.9 for the Cr-Co-Ni MEA to ~0.7 for the Cr-Fe-Co-Ni HEA, when [$\bar{1}$23]-oriented single crystals are deformed in tension at 77 K (Fig. 12). This is consistent with the experimental fact that the extent of overshoot is not simply inversely related to stacking fault energy, as described in the section 3.2.1. This clearly indicates that the twinning stress (τ_{twin}) cannot be determined only with intrinsic materials parameters such as γ_{isf} and b_{twin} but it contains the contribution from some extrinsic parameters that may be related, for example, to deformation history prior to deformation twinning. We believe that this corresponds to the third term of equation (7).

4.3.2. Twinning stress and comparison with some model predictions

Kibey et al. proposed a model for deformation twinning in FCC metals and alloys, incorporating the generalized stacking fault energy (GSFE) calculated by first-principles methods (Kibey et al., 2007a, 2007b, 2009). The model considers the total energy associated with the Mahajan-Chin three-layer twin nucleus (Mahajan and Chin, 1973) due to the (i) elastic energy of dislocations bounding the nucleus, (ii) misfit energy associated with the twinning energy pathway (the integration of the GSFE) and (iii) work

done by applied shear stress. We estimated the twinning shear stress (τ_{twin}) of the present three HEA/MEAs with the model by Kibey et al. (Kibey et al., 2007a, 2007b, 2009) using the GSFE values of FCC HEA/MEAs calculated by Huang et al. (Huang et al., 2018), as shown in Fig. 13. The experimentally-determined twinning shear stresses for the three HEA/MEAs are plotted as a function of unstable twinning fault energy (γ_{ut}) together with data for some pure FCC metals. While the model successfully predicts the τ_{twin} of some pure FCC metals, it significantly underestimates the τ_{twin} values of the present HEA/MEAs (Fig. 13).

Huang et al. (Huang et al., 2018) then modified the model by Kibey et al. (Kibey et al., 2007a, 2007b, 2009) by ignoring the contribution from the elastic energy of dislocations bounding the nucleus and predicted the twinning stress for the equiatomic Cr-Fe-Co-Ni MEA to be 274 MPa, which agrees well with the experimentally-determined value (249 MPa) in the present study (Fig. 13). However, the model of Huang et al. (Huang et al., 2018) underestimates the twinning shear stress for the equiatomic Cr-Mn-Fe-Co-Ni HEA and Cr-Co-Ni MEA (Fig. 13). This may indicate again that the twinning stress (τ_{twin}) cannot be determined only with intrinsic materials parameters such as γ_{isf} and γ_{ut} and contributions from some extrinsic parameters that are related to deformation history prior to deformation twinning must be taken into account.

5. Conclusions

The plastic deformation behavior of single crystals of the equiatomic Cr-Fe-Co-Ni MEA was investigated as a function of temperature and compared with the behaviors of the Cr-Mn-Fe-Co-Ni HEA and Cr-Co-Ni MEA. The following conclusions are drawn from the present study.

(1) The CRSS for $\{111\}\langle 1\bar{1}0\rangle$ slip is 44-45 MPa and 99-102 MPa at room temperature and 77 K, respectively, and do not exhibit any tension-compression asymmetry. A dulling of the temperature dependence of CRSS, which may be due to the inertia effect, is observed below 77 K. The CRSS at 0 K is estimated to be 200 MPa by extrapolating from CRSS values above 77 K where the inertia effect is absent. This 0 K CRSS is in between those of the equiatomic Cr-Mn-Fe-Ni-Co HEA and Cr-Co-Ni MEA (174 and 225 MPa, respectively). These CRSS values agree well with predictions of the model of Toda-Caraballo et al. and the MSAD model.

(2) Although the temperature dependence of CRSS at cryogenic temperatures is much steeper for these HEA and MEAs than conventional binary FCC solid-solution alloys, the activation enthalpy for deformation at room temperature in all cases falls within a narrow range of 0.6~0.7 eV, indicating a likely similarity of thermally activated dislocation motion regardless of whether they are HEA/MEAs or conventional binary alloys.

(3) The stacking fault energy of the equiatomic Cr-Fe-Co-Ni MEA estimated from the separation distances between coupled Shockley partial dislocations is about 20 mJ/m^{-2}, which is in between those of the equiatomic Cr-Mn-Fe-Ni-Co HEA and Cr-Ni-Co MEA (30 and 14 mJ/m^{-2}, respectively) and is sufficiently low to account for the planar dislocation arrays and the occurrence of deformation twinning at 77 K.

(4) Deformation twinning occurs at 77 K at a high plastic strain of about 110%. Twinning occurs on conjugate $(\bar{1}\bar{1}1)$ planes in the form of Lüders deformation after the tensile axis overshoots to $[\bar{1}3,12,25]$ at an onset twinning shear stress of 249 MPa. The relationship between the twinning stress and stacking fault energy is not monotonic as previously believed; rather, it has a concave upward shape with a minimum twinning stress at an intermediate value of stacking fault energy.

Acknowledgements

This work was supported by Grant-in-Aids for Scientific Research on innovative Areas on High Entropy Alloys through the grant number JP18H05450 and JP18H05451, in part by JSPS KAKENHI (grant numbers JP18H05478, JP21H01651, JP21K18825 and JP22H00262), the Elements Strategy Initiative for Structural Materials (ESISM) from the Ministry of Education, Culture, Sports, Science and Technology (MEXT) of Japan (grant number JPMXP0112101000), JST CREST (grant number JPMJCR1994), and JST Spring (grant number JPMJSP2110). Dr. A. Equbal of Kyoto University is greatly acknowledged for his help in experiment. HI and MH acknowledge the support from the Alexander von Humboldt Foundation for their cooperative research conducted under the Humboldt Fellowship of HI.

Reference

Bahramyan, M., Mousavian, R.T., Brabazon, D., 2020. Study of the plastic deformation mechanism of TRIP–TWIP high entropy alloys at the atomic level. Int. J. Plast. 127, 102649. https://doi.org/10.1016/j.ijplas.2019.102649

Basinski, Z.S., Foxall, R.A., Pascual, R., 1972. Stress equivalence of solution hardening. Scr. Metall. 6, 807–814. https://doi.org/10.1016/0036-9748(72)90052-X

Bertoli, G., Otani, L.B., Clarke, A.J., Kiminami, C.S., Coury, F.G., 2021. Hall–Petch and grain growth kinetics of the low stacking fault energy TRIP $Cr_{40}Co_{40}Ni_{20}$ multi-principal element alloy. Appl. Phys. Lett. 119, 061903. https://doi.org/10.1063/5.0057888

Bracq, G., Laurent-Brocq, M., Varvenne, C., Perrière, L., Curtin, W.A., Joubert, J.M., Guillot, I., 2019. Combining experiments and modeling to explore the solid solution strengthening of high and medium entropy alloys. Acta Mater. 177, 266–279.

https://doi.org/10.1016/j.actamat.2019.06.050
Butt, M.Z., Feltham, P., 1978. Solid-solution hardening. Acta Metall. 26, 167–173. https://doi.org/10.1016/0001-6160(78)90213-4
Butt, M.Z., Feltham, P., 1993. Solid-solution hardening. J. Mater. Sci. 28, 2557–2576. https://doi.org/10.1007/BF00356192
Butt, M.Z., 1998. Investigation of the activation-parameters of low-temperature slip in cubic metals. Czechoslov. J. Phys. 49, 1177–1184. https://doi.org/10.1023/A:1021126232107
Christian, J.W., Mahajan, S., 1995. Deformation twinning. Prog. Mater. Sci. 39, 1–157. https://doi.org/10.1016/0079-6425(94)00007-7
Cockayne, D.J.H., Jenkins, M.L., Ray, I.L.F., 1971. The measurement of stacking-fault energies of pure face-centred cubic metals. Philos. Mag. 24, 1383–1392. https://doi.org/10.1080/14786437108217419
Conrad, H., 1964. Thermally activated deformation of metals. JOM 16, 582–588. https://doi.org/10.1007/BF03378292
Coury, F.G., Clarke, K.D., Kiminami, C.S., Kaufman, M.J., Clarke, A.J., 2018. High Throughput Discovery and Design of Strong Multicomponent Metallic Solid Solutions. Sci. Rep. 8, 1–10. https://doi.org/10.1038/s41598-018-26830-6
Fan, Z., Li, L., Chen, Z., Asakura, M., Zhang, C., Yang, Z., Inui, H., George, E.P., 2023. Temperature-dependent yield stress of single crystals of non-equiatomic Cr-Mn-Fe-Co-Ni high-entropy alloys in the temperature range 10-1173 K. Acta Mater. 246, 118712. https://doi.org/10.1016/j.actamat.2023.118712
Gali, A., George, E.P., 2013. Tensile properties of high- and medium-entropy alloys. Intermetallics 39, 74–78. https://doi.org/10.1016/j.intermet.2013.03.018
George, E.P., Curtin, W.A., Tasan, C.C., 2020. High entropy alloys: A focused review of mechanical properties and deformation mechanisms. Acta Mater. 188, 435–474. https://doi.org/10.1016/j.actamat.2019.12.015
George, E.P., Raabe, D., Ritchie, R.O., 2019. High-entropy alloys. Nat. Rev. Mater. 4, 515–534. https://doi.org/10.1038/s41578-019-0121-4
Gludovatz, B., Hohenwarter, A., Catoor, D., Chang, E.H., George, E.P., Ritchie, R.O., 2014. A fracture-resistant high-entropy alloy for cryogenic applications. Science. 345, 1153–1158. https://doi.org/10.1126/science.1254581
Gludovatz, B., Hohenwarter, A., Thurston, K.V.S., Bei, H., Wu, Z., George, E.P., Ritchie, R.O., 2016. Exceptional damage-tolerance of a medium-entropy alloy CrCoNi at cryogenic temperatures. Nat. Commun. 7, 10602. https://doi.org/10.1038/ncomms10602
Granato, A. V., 1971. Dislocation Inertial Effects in the Plasticity of Superconductors.

Phys. Rev. B 4, 2196–2201. https://doi.org/10.1103/PhysRevB.4.2196

Gupta, A., Jian, W.-R., Xu, S., Beyerlein, I.J., Tucker, G.J., 2022. On the deformation behavior of CoCrNi medium entropy alloys: Unraveling mechanistic competition. Int. J. Plast. 159, 103442. https://doi.org/10.1016/j.ijplas.2022.103442

Gypen, L.A., Deruyttere, A., 1977a. Multi-component solid solution hardening: Part 1 Proposed model. J. Mater. Sci. 12, 1028–1033. https://doi.org/10.1007/BF00540987

Gypen, L.A., Deruyttere, A., 1977b. Multi-component solid solution hardening: Part 2 Agreement with experimental results. J. Mater. Sci. 12, 1034–1038. https://doi.org/10.1007/BF00540988

Hashimoto, N., Fukushi, T., Wada, E., Chen, W.-Y., 2021. Effect of stacking fault energy on damage microstructure in ion-irradiated CoCrFeNiMn concentrated solid solution alloys. J. Nucl. Mater. 545, 152642. https://doi.org/10.1016/j.jnucmat.2020.152642

Hua, D., Xia, Q., Wang, W., Zhou, Q., Li, S., Qian, D., Shi, J., Wang, H., 2021. Atomistic insights into the deformation mechanism of a CoCrNi medium entropy alloy under nanoindentation. Int. J. Plast. 142, 102997. https://doi.org/10.1016/J.IJPLAS.2021.102997

Huang, H., Li, X., Dong, Z., Li, W., Huang, S., Meng, D., Lai, X., Liu, T., Zhu, S., Vitos, L., 2018. Critical stress for twinning nucleation in CrCoNi-based medium and high entropy alloys. Acta Mater. 149, 388–396. https://doi.org/10.1016/j.actamat.2018.02.037

Inui, H., Kishida, K., Chen, Z., 2022a. Recent Progress in Our Understanding of Phase Stability, Atomic Structures and Mechanical and Functional Properties of High-Entropy Alloys. Mater. Trans. 63, MT-M2021234. https://doi.org/10.2320/matertrans.MT-M2021234

Inui, H., Kishida, K., Li, L., Manzoni, A.M., Haas, S., Glatzel, U., 2022b. Uniaxial mechanical properties of face-centered cubic single- and multiphase high-entropy alloys. MRS Bull. 1–7. https://doi.org/10.1557/S43577-022-00280-Y

Jax, P., Kratochvil, P., Haasen, P., 1970. Solid solution hardening of gold and other f.c.c. single crystals. Acta Metall. 18, 237–245. https://doi.org/10.1016/0001-6160(70)90029-5

Kawamura, M., Asakura, M., Okamoto, N.L., Kishida, K., Inui, H., George, E.P., 2021. Plastic deformation of single crystals of the equiatomic Cr−Mn−Fe−Co−Ni high-entropy alloy in tension and compression from 10 K to 1273 K. Acta Mater. 203, 116454. https://doi.org/10.1016/j.actamat.2020.10.073

Kibey, S., Liu, J.B., Johnson, D.D., Sehitoglu, H., 2007a. Predicting twinning stress in fcc metals: Linking twin-energy pathways to twin nucleation. Acta Mater. 55, 6843–

6851. https://doi.org/10.1016/j.actamat.2007.08.042

Kibey, S., Liu, J.B., Johnson, D.D., Sehitoglu, H., 2007b. Energy pathways and directionality in deformation twinning. Appl. Phys. Lett. 91, 181916. https://doi.org/10.1063/1.2800806

Kibey, S.A., Wang, L.L., Liu, J.B., Johnson, H.T., Sehitoglu, H., Johnson, D.D., 2009. Quantitative prediction of twinning stress in fcc alloys: Application to Cu-Al. Phys. Rev. B 79, 214202. https://doi.org/10.1103/PhysRevB.79.214202

Kim, J.K., Kim, J.H., Park, H., Kim, J.S., Yang, G., Kim, R., Song, T., Suh, D.W., Kim, J., 2022. Temperature-dependent universal dislocation structures and transition of plasticity enhancing mechanisms of the Fe40Mn40Co10Cr10 high entropy alloy. Int. J. Plast. 148, 103148. https://doi.org/10.1016/j.ijplas.2021.103148

Kocks, U.F., Argon, A.S., Ashby, M.F., 1975. Thermodynamics and Kinetics of Slip. Prog. Mater. Sci. 19, 1–291.

Kresse, G., Furthmüller, J., 1996. Efficient iterative schemes for ab initio total-energy calculations using a plane-wave basis set. Phys. Rev. B 54, 11169–11186. https://doi.org/10.1103/PhysRevB.54.11169

Labusch, R., 1970. A Statistical Theory of Solid Solution Hardening. Phys. status solidi 41, 659–669. https://doi.org/10.1002/pssb.19700410221

Laplanche, G., Gadaud, P., Bärsch, C., Demtröder, K., Reinhart, C., Schreuer, J., George, E.P., 2018. Elastic moduli and thermal expansion coefficients of medium-entropy subsystems of the CrMnFeCoNi high-entropy alloy. J. Alloys Compd. 746, 244–255. https://doi.org/10.1016/j.jallcom.2018.02.251

Laplanche, G., Gadaud, P., Horst, O., Otto, F., Eggeler, G., George, E.P., 2015. Temperature dependencies of the elastic moduli and thermal expansion coefficient of an equiatomic, single-phase CoCrFeMnNi high-entropy alloy. J. Alloys Compd. 623, 348–353. https://doi.org/10.1016/j.jallcom.2014.11.061

Laplanche, G., Kostka, A., Horst, O.M., Eggeler, G., George, E.P., 2016. Microstructure evolution and critical stress for twinning in the CrMnFeCoNi high-entropy alloy. Acta Mater. 118, 152–163. https://doi.org/10.1016/j.actamat.2016.07.038

Laplanche, G., Kostka, A., Reinhart, C., Hunfeld, J., Eggeler, G., George, E.P., 2017. Reasons for the superior mechanical properties of medium-entropy CrCoNi compared to high-entropy CrMnFeCoNi. Acta Mater. 128, 292–303. https://doi.org/10.1016/j.actamat.2017.02.036

Li, L., Chen, Z., Kuroiwa, S., Ito, M., Kishida, K., Inui, H., George, E.P., 2022. Tensile and compressive plastic deformation behavior of medium-entropy Cr-Co-Ni single crystals from cryogenic to elevated temperatures. Int. J. Plast. 148, 103144. https://doi.org/10.1016/J.IJPLAS.2021.103144

Li, L., Chen, Z., Kuroiwa, S., Ito, M., Yuge, K., Kishida, K., Tanimoto, H., Yu, Y., Inui, H., George, E.P., 2023. Evolution of short-range order and its effects on the plastic deformation behavior of single crystals of the equiatomic Cr-Co-Ni medium-entropy alloy. Acta Mater. 243, 118537. https://doi.org/10.1016/j.actamat.2022.118537

Li, Z., Ma, S., Zhao, S., Zhang, W., Peng, F., Li, Q., Yang, T., Wu, C.-Y., Wei, D., Chou, Y.-C., Liaw, P.K., Gao, Y., Wu, Z., 2023. Achieving superb strength in single-phase FCC alloys via maximizing volume misfit. Mater. Today 63, 108–119. https://doi.org/10.1016/j.mattod.2023.02.012

Li, Z., Zhao, S., Ritchie, R.O., Meyers, M.A., 2019. Mechanical properties of high-entropy alloys with emphasis on face-centered cubic alloys. Prog. Mater. Sci. 102, 296–345. https://doi.org/https://doi.org/10.1016/j.pmatsci.2018.12.003

Liu, D., Yu, Q., Kabra, S., Jiang, M., Forna-Kreutzer, P., Zhang, R., Payne, M., Walsh, F., Gludovatz, B., Asta, M., Minor, A.M., George, E.P., Ritchie, R.O., 2022. Exceptional fracture toughness of CrCoNi-based medium- and high-entropy alloys at 20 kelvin. Science. 378, 978–983. https://doi.org/10.1126/science.abp8070

Liu, S.F., Wu, Y., Wang, H.T., He, J.Y., Liu, J.B., Chen, C.X., Liu, X.J., Wang, H., Lu, Z.P., 2018. Stacking fault energy of face-centered-cubic high entropy alloys. Intermetallics 93, 269–273. https://doi.org/10.1016/j.intermet.2017.10.004

Mahajan, S., Chin, G.Y., 1973. Formation of deformation twins in f.c.c. crystals. Acta Metall. 21, 1353–1363. https://doi.org/10.1016/0001-6160(73)90085-0

Miao, J., Slone, C.E., Smith, T.M., Niu, C., Bei, H., Ghazisaeidi, M., Pharr, G.M., Mills, M.J., 2017. The evolution of the deformation substructure in a Ni-Co-Cr equiatomic solid solution alloy. Acta Mater. 132, 35–48. https://doi.org/10.1016/j.actamat.2017.04.033

Miracle, D.B., Senkov, O.N., 2017. A critical review of high entropy alloys and related concepts. Acta Mater. 122, 448–511. https://doi.org/10.1016/j.actamat.2016.08.081

Naeem, M., He, H., Harjo, S., Kawasaki, T., Lin, W., Kai, J.J., Wu, Z., Lan, S., Wang, X.L., 2021. Temperature-dependent hardening contributions in CrFeCoNi high-entropy alloy. Acta Mater. 221, 117371. https://doi.org/10.1016/j.actamat.2021.117371

Naeem, M., He, H., Zhang, F., Huang, H., Harjo, S., Kawasaki, T., Wang, B., Lan, S., Wu, Z., Wang, F., Wu, Y., Lu, Z., Zhang, Z., Liu, C.T., Wang, X.-L., 2020. Cooperative deformation in high-entropy alloys at ultralow temperatures. Sci. Adv. 6, eaax4002. https://doi.org/10.1126/sciadv.aax4002

Nöhring, W.G., Curtin, W.A., 2019. Correlation of microdistortions with misfit volumes in High Entropy Alloys. Scr. Mater. 168, 119–123.

https://doi.org/10.1016/j.scriptamat.2019.04.012

Okamoto, N.L., Fujimoto, S., Kambara, Y., Kawamura, M., Chen, Z.M.T., Matsunoshita, H., Tanaka, K., Inui, H., George, E.P., 2016a. Size effect, critical resolved shear stress, stacking fault energy, and solid solution strengthening in the CrMnFeCoNi high-entropy alloy. Sci. Rep. 6, 35863. https://doi.org/10.1038/srep35863

Okamoto, N.L., Yuge, K., Tanaka, K., Inui, H., George, E.P., 2016b. Atomic displacement in the CrMnFeCoNi high-entropy alloy – A scaling factor to predict solid solution strengthening. AIP Adv. 6, 125008. https://doi.org/10.1063/1.4971371

Rodriguez, P., 1984. Serrated plastic flow. Bull. Mater. Sci. 6, 653–663. https://doi.org/10.1007/BF02743993

Schwarz, R.B., Isaac, R.D., Granato, A. V., 1977. Dislocation Inertial Effects in the Plastic Deformation of Dilute Alloys of Lead and Copper. Phys. Rev. Lett. 38, 554–557. https://doi.org/10.1103/PhysRevLett.38.554

Sohn, S.S., Kwiatkowski da Silva, A., Ikeda, Y., Körmann, F., Lu, W., Choi, W.S., Gault, B., Ponge, D., Neugebauer, J., Raabe, D., 2019. Ultrastrong Medium-Entropy Single-Phase Alloys Designed via Severe Lattice Distortion. Adv. Mater. 31, 1807142. https://doi.org/10.1002/adma.201807142

Stobbs, W.M., Sworn, C.H., 1971. The weak beam technique as applied to the determination of the stacking-fault energy of copper. Philos. Mag. 24, 1365–1381. https://doi.org/10.1080/14786437108217418

Suzuki, H., Kuramoto, E., 1968. Thermally activated glide in face-centered cubic alloys. Trans JIM. 9, Suppl. 697–702.

Szczerba, M.J., Szczerba, M.S., 2017. Slip versus twinning in low and very low stacking-fault energy Cu-Al alloy single crystals. Acta Mater. 133, 109–119. https://doi.org/10.1016/j.actamat.2017.05.011

Toda-Caraballo, I., 2017. A general formulation for solid solution hardening effect in multicomponent alloys. Scr. Mater. 127, 113–117. https://doi.org/10.1016/j.scriptamat.2016.09.009

Toda-Caraballo, I., Rivera-Díaz-del-Castillo, P.E.J., 2015. Modelling solid solution hardening in high entropy alloys. Acta Mater. 85, 14–23. https://doi.org/10.1016/j.actamat.2014.11.014

Tsai, C.W., Lee, C., Lin, P.T., Xie, X., Chen, S., Carroll, R., Leblanc, M., Brinkman, B.A.W., Liaw, P.K., Dahmen, K.A., Yeh, J.W., 2019. Portevin-Le Chatelier mechanism in face-centered-cubic metallic alloys from low to high entropy. Int. J. Plast. 122, 212–224. https://doi.org/10.1016/j.ijplas.2019.07.003

Varvenne, C.C., Luque, A., Curtin, W.A., 2016. Theory of strengthening in fcc high

entropy alloys. Acta Mater. 118, 164–176. https://doi.org/10.1016/j.actamat.2016.07.040

Venables, J.A., 1964. Deformation twinning in fcc metals, in: Reed-Hill, R.E., Hirth, J.P., Rogers, H.C. (Eds.), Deformation Twinning. Gordon and Breach Science Publishers, New York, pp. 77–116.

Wagner, C., Ferrari, A., Schreuer, J., Couzinié, J.-P., Ikeda, Y., Körmann, F., Eggeler, G., George, E.P., Laplanche, G., 2022. Effects of Cr/Ni ratio on physical properties of Cr-Mn-Fe-Co-Ni high-entropy alloys. Acta Mater. 227, 117693. https://doi.org/10.1016/j.actamat.2022.117693

Wagner, C., Laplanche, G., 2023. Effects of stacking fault energy and temperature on grain boundary strengthening, intrinsic lattice strength and deformation mechanisms in CrMnFeCoNi high-entropy alloys with different Cr/Ni ratios. Acta Mater. 244, 118541. https://doi.org/10.1016/j.actamat.2022.118541

Wang, X., De Vecchis, R.R., Li, C., Zhang, H., Hu, X., Sridar, S., Wang, Y., Chen, W., Xiong, W., 2022. Design metastability in high-entropy alloys by tailoring unstable fault energies. Sci. Adv. 8. https://doi.org/10.1126/sciadv.abo7333

Wang, Y., Liu, B., Yan, K., Wang, M., Kabra, S., Chiu, Y.-L., Dye, D., Lee, P.D., Liu, Y., Cai, B., 2018. Probing deformation mechanisms of a FeCoCrNi high-entropy alloy at 293 and 77 K using in situ neutron diffraction. Acta Mater. 154, 79–89. https://doi.org/10.1016/j.actamat.2018.05.013

Wang, Z., Li, L., Chen, Z., Yuge, K., Kishida, K., Inui, H., Heilmaier, M., 2023. A new route to achieve high strength and high ductility compositions in Cr-Co-Ni-based medium-entropy alloys: A predictive model connecting theoretical calculations and experimental measurements. J. Alloys Compd. 170555. https://doi.org/10.1016/j.jallcom.2023.170555

Wei, D., Li, X., Schönecker, S., Jiang, J., Choi, W.M., Lee, B.J., Kim, H.S., Chiba, A., Kato, H., 2019. Development of strong and ductile metastable face-centered cubic single-phase high-entropy alloys. Acta Mater. 181, 318–330. https://doi.org/10.1016/j.actamat.2019.09.050

Wei, D., Gong, W., Tsuru, T., Kawasaki, T., Harjo, S., Cai, B., Liaw, P.K., Kato, H., 2022a. Mechanical behaviors of equiatomic and near-equiatomic face-centered-cubic phase high-entropy alloys probed using in situ neutron diffraction. Int. J. Plast. 158, 103417. https://doi.org/10.1016/j.ijplas.2022.103417

Wei, D., Gong, W., Tsuru, T., Lobzenko, I., Li, X., Harjo, S., Kawasaki, T., Do, H., Wung, J., Wagner, C., Laplanche, G., Koizumi, Y., Adachi, H., Aoyagi, K., Chiba, A., Lee, B., Seop, H., 2022b. Si-addition contributes to overcoming the strength-ductility trade-off in high-entropy alloys. Int. J. Plast. 159, 103443.

https://doi.org/10.1016/j.ijplas.2022.103443

Wessels, E.J.H., Nabarro, F.R.N., 1971. A theory of unstable glide in the presence of a dense dislocation forest. Acta Metall. 19, 915–921. https://doi.org/10.1016/0001-6160(71)90084-8

Wille, T.H., Gieseke, W., Schwink, C.H., 1987. Quantitative analysis of solution hardening in selected copper alloys. Acta Metall. 35, 2679–2693. https://doi.org/10.1016/0001-6160(87)90267-7

Wille, T.H., Schwink, C., 1986. Precision measurements of critical resolved shear stress in CuMn alloys. Acta Metall. 34, 1059–1069. https://doi.org/10.1016/0001-6160(86)90216-6

Wu, Z., Gao, Y.F., Bei, H., 2015. Single crystal plastic behavior of a single-phase, face-center-cubic-structured, equiatomic FeNiCrCo alloy. Scr. Mater. 109, 108–112. https://doi.org/10.1016/j.scriptamat.2015.07.031

Yan, J.X., Zhang, Z.J., Zhang, P., Liu, J.H., Yu, H., Hu, Q.M., Yang, J.B., Zhang, Z.F., 2023. Design and optimization of the composition and mechanical properties for non-equiatomic CoCrNi medium-entropy alloys. J. Mater. Sci. Technol. 139, 232–244. https://doi.org/10.1016/j.jmst.2022.07.031

Zhang, T.W., Ma, S.G., Zhao, D., Wu, Y.C., Zhang, Y., Wang, Z.H., Qiao, J.W., 2020. Simultaneous enhancement of strength and ductility in a NiCoCrFe high-entropy alloy upon dynamic tension: Micromechanism and constitutive modeling. Int. J. Plast. 124, 226–246. https://doi.org/10.1016/j.ijplas.2019.08.013

Zhang, X., Gui, Y., Lai, M., Lu, X., Gu, J., Wang, F., Yang, T., Wang, Z., Song, M., 2023. Enhanced strength-ductility synergy of medium-entropy alloys via multiple level gradient structures. Int. J. Plast. 164, 103592. https://doi.org/10.1016/j.ijplas.2023.103592

Zhang, Z.J., Mao, M.M., Wang, J., Gludovatz, B., Zhang, Ze, Mao, S.X., George, E.P., Yu, Q., Ritchie, R.O., 2015. Nanoscale origins of the damage tolerance of the high-entropy alloy CrMnFeCoNi. Nat. Commun. 6, 10143. https://doi.org/10.1038/ncomms10143

Zhang, Z.J., Sheng, H., Wang, Z., Gludovatz, B., Zhang, Ze, George, E.P., Yu, Q., Mao, S.X., Ritchie, R.O., 2017. Dislocation mechanisms and 3D twin architectures generate exceptional strength-ductility-toughness combination in CrCoNi medium-entropy alloy. Nat. Commun. 8, 14390. https://doi.org/10.1038/ncomms14390

Zhao, S., Stocks, G.M., Zhang, Y., 2017. Stacking fault energies of face-centered cubic concentrated solid solution alloys. Acta Mater. 134, 334–345. https://doi.org/10.1016/j.actamat.2017.05.001

Zunger, A., Wei, S.-H.S.-H., Ferreira, L.G., Bernard, J.E., 1990. Special quasirandom

structures. Phys. Rev. Lett. 65, 353–356.
https://doi.org/10.1103/PhysRevLett.65.353

Figure Captions

Fig. 1. Temperature dependence of CRSS for [$\bar{1}$23]-oriented single-crystals of the equiatomic Cr-Fe-Co-Ni MEA from 10 K to 1373 K in compression at a strain rate of 1×10^{-4} s^{-1}. Results for the equiatomic Cr-Mn-Fe-Co-Ni HEA (Kawamura et al., 2021) and equiatomic Cr-Co-Ni MEA (Li et al., 2022) are also plotted for comparison.

Fig. 2. (a) The strain-rate sensitivity of flow stress measured at selected temperatures for [$\bar{1}$23]-oriented single crystals of the equiatomic Cr-Fe-Co-Ni MEA. (b) The gradient of the strain-rate sensitivity shown in (a) plotted as a function of temperature.

Fig. 3. (a) TEM bright-field and (b) weak-beam dark-field images of the equiatomic Cr-Fe-Co-Ni MEA deformed to about 2~3% plastic strain at room temperature. The thin foil was cut parallel to the (111) primary slip plane. (c) Dissociation widths of coupled Shockley partial dislocations plotted as a function of angle (θ) between the Burgers vector and dislocation line.

Fig. 4. (a) Engineering stress-strain and (b) true stress-strain curves for [$\bar{1}$23]-oriented single crystals of the equiatomic Cr-Fe-Co-Ni MEA deformed to failure in tension at 77 K and room temperature. (c) Work hardening rate for [$\bar{1}$23]-oriented single crystals of the equiatomic Cr-Fe-Co-Ni MEA calculated from (b) as a function of true strain.

Fig. 5. (a) Tensile engineering stress-strain curve for a [$\bar{1}$23]-oriented single crystal of the equiatomic Cr-Fe-Co-Ni MEA deformed in tension at 77 K, in which the test was repeatedly interrupted at points A-D for microstructure observations. (b) EBSD orientation maps at the interruptions A-D with enlargements of the framed areas shown on the right-hand side for C-D. (c) Stereographic projection of the tensile-axis rotation during deformation. (d) Misorientation along the points X and Y in frame D1 in (b), showing the existence of deformation twins.

Fig. 6. (a) Typical dark-field TEM image of deformation twins in a [$\bar{1}$23]-oriented single crystal of the Cr-Fe-Co-Ni MEA deformed to failure at 77 K. The thin foil was cut perpendicular to the ($\bar{1}\bar{1}$1) conjugate twinning planes. (b) Thickness distribution histogram of twins measured with dark-field TEM images. (c) Atomic-resolution STEM image of deformation twins in a [$\bar{1}$23]-oriented single crystal deformed to failure at 77 K. (d) Thickness distribution histograms of

twins and HCP layers measured with atomic-resolution STEM images.

Fig. 7. (a) Temperature dependence of activation volume for deformation of single crystals of the three HEA/MEAs and (b) activation volumes of the three HEA/MEAs after fitting with equation (3). (c) Activation volumes plotted as a function of Cr content at selected temperatures. (d) The activation enthalpies for deformation estimated with the equation (4) plotted as a function of shear stress.

Fig. 8. (a) Difference between the yield stress at 77 K and that at room temperature plotted as a function of the yield stress at 77 K for FCC solid solutions and the three HEA/MEAs. (b) Activation volumes at 77 K and room temperature for FCC solid solutions and the three HEA/MEAs.

Fig. 9. (a) Contributions from the size misfit term and modulus misfit term to the 0 K CRSS estimated with equation (5) and (b) 0 K CRSS predicted with equation (6) and $Z = 3.030$ for the equiatomic Cr-Fe-Co-Ni MEA (this study), the equiatomic Cr-Mn-Fe-Co-Ni HEA (Kawamura et al., 2021) and the Cr-Co-Ni MEA (Li et al., 2022).

Fig. 10. (a) MSAD for each of the constituent elements and averaged values for the three alloys. (b) Relation between the experimental 0 K CRSS and MSAD for the three HEA/MEAs. The 0 K CRSS and MSAD are normalized by the shear modulus and dislocation Burgers vector, respectively.

Fig. 11. (a) Relationship between the twinning shear stress at 77 K and stacking fault energy for $[\bar{1}23]$-oriented single crystals (solid symbols) and polycrystals (open symbols) of the equiatomic Cr-Mn-Fe-Co-Ni HEA and Cr-Fe-Co-Ni and Cr-Co-Ni MEAs, together with that reported previously for FCC slid-solution alloys. (b) The estimated contributions to the twinning shear stress from the three terms in equation (7) plotted as a function of stacking fault energy for the three HEA/MEAs.

Fig. 12. True strain at the onset of deformation twinning at 77 K plotted as a function of stacking fault energy for the three HEA/MEAs.

Fig. 13. Twinning shear stress of the three HEA/MEAs plotted as a function of unstable stacking fault energy calculated by Huang et al. (Huang et al., 2018): experimentally determined values for $[\bar{1}23]$-oriented single crystals (solid symbols), predicted values from models by Kibey et al. (Kibey et al., 2007a) (open symbols) and Huang et al. (Huang et al., 2018) (open with cross symbols). The data points for some pure FCC metals are also shown for comparison (Kibey et al., 2007a).

Table 1 Cr content (c_{Cr}) and experimental 0 K CRSS values (τ_0) for the equiatomic Cr-Fe-Co-Ni MEA (this study), the equiatomic Cr-Mn-Fe-Co-Ni HEA (Kawamura et al., 2021) and Cr-Co-Ni MEA (Li et al., 2022), determined by fitting the CRSS-temperature curves with equation (1) using optimal parameters (T_a, $1/p$ and $1/q$). The 0 K activation volumes (V_0) and material-dependent constant (W_0) obtained by fitting the activation volume-temperature curves of Fig. 7(a) with equation (3).

	c_{Cr}	τ_0 (MPa)	T_a (K)	$1/q$	$1/p$	V_0 (b^3)	W_0 (10^{-19} J)
Cr-Mn-Fe-Co-Ni	0.20	174	873	0.82	3.56	22.97	0.794
Cr-Fe-Co-Ni	0.25	200	873	0.50	2.20	21.87	0.966
Cr-Co-Ni	0.33	225	873	0.66	2.66	20.49	1.130

Figure captions for supplementary figures

Fig. S1. Compressive stress-strain curves at selected temperatures for $[\bar{1}23]$-oriented single crystals of the equiatomic Cr-Fe-Co-Ni MEA. Compression tests were usually started at a strain rate of 1×10^{-4} s^{-1} to determine the yield stress and then strain-rate sensitivity was measured by strain-rate jump tests as indicated with arrows (at room temperature and below).

Fig. S2. Deformation markings observed on two orthogonal side surfaces ((a,c) $(1\bar{1}1)$ and (b,d) $(54\bar{1})$) of $[\bar{1}23]$-oriented single crystals deformed in compression at (a,b) 77 K and (c, d) room temperature.

Fig. S3. Tensile and compressive stress-strain curves at 77 K and room temperature for $[\bar{1}23]$-oriented single crystals of the equiatomic Cr-Fe-Co-Ni MEA.

Fig. S4. EBSD orientation map of a $[\bar{1}23]$-oriented single crystal of the equiatomic Cr-Fe-Co-Ni MEA deformed in tension to failure at room temperature. There is no indication that deformation twinning occurred.

Fig. S5. Twin thickness distribution in $[\bar{1}23]$-oriented single crystals of the equiatomic Cr-Mn-Fe-Co-Ni HEA deformed in tension to failure at 77 K measure from dark-field TEM images (Kawamura et al., 2021).

Fig. S6. (a) The stacking fault energy (right Y axis) and the twinning shear stress at 77 K (left Y axis) plotted as against Cr content for $[\bar{1}23]$-oriented single crystals of the equiatomic Cr-Mn-Fe-Co-Ni HEA and Cr-Fe-Co-Ni and Cr-Co-Ni MEAs. (b) The estimated contributions to the twinning shear stress from the three terms in equation (7) plotted as a function of Cr content for the three HEA/MEAs.

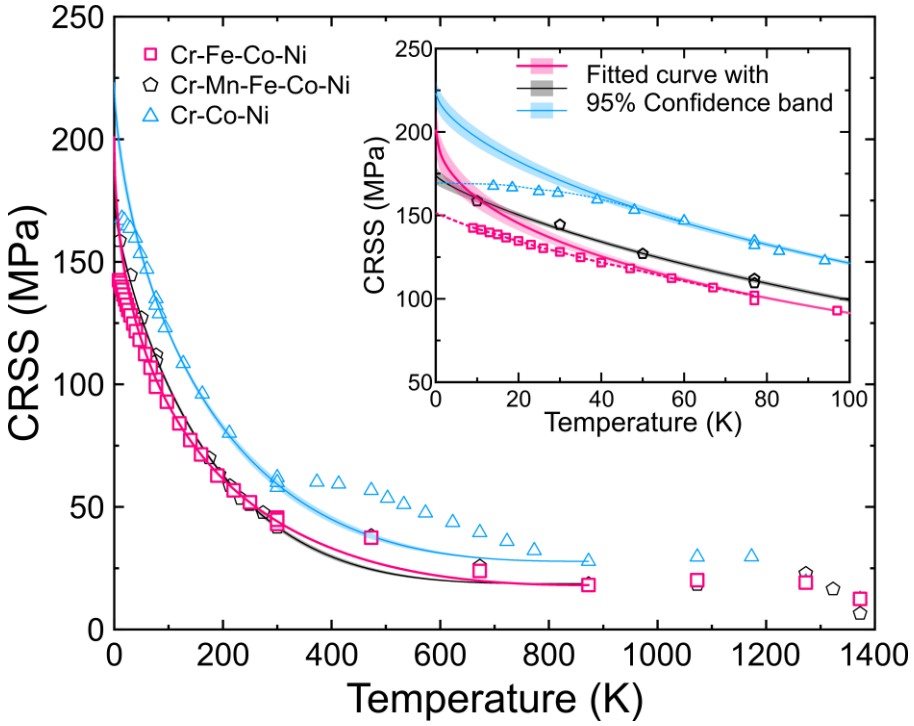

Fig. 1. Temperature dependence of CRSS for [$\bar{1}$23]-oriented single-crystals of the equiatomic Cr-Fe-Co-Ni MEA from 10 K to 1373 K in compression at a strain rate of 1×10^{-4} s^{-1}. Results for the equiatomic Cr-Mn-Fe-Co-Ni HEA (Kawamura et al., 2021) and equiatomic Cr-Co-Ni MEA (Li et al., 2022) are also plotted for comparison.

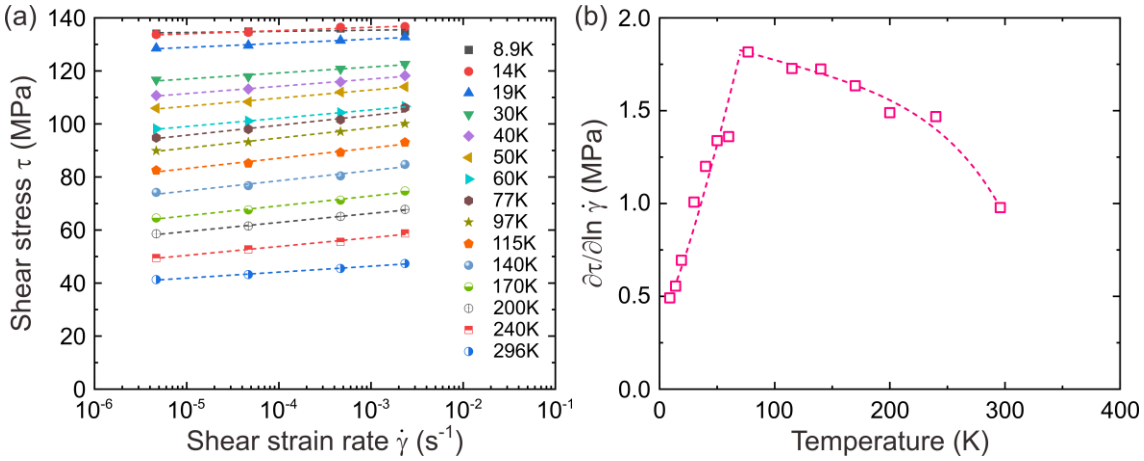

Fig. 2. (a) The strain-rate sensitivity of flow stress measured at selected temperatures for [$\bar{1}$23]-oriented single crystals of the equiatomic Cr-Fe-Co-Ni MEA. (b) The gradient of the strain-rate sensitivity shown in (a) plotted as a function of temperature.

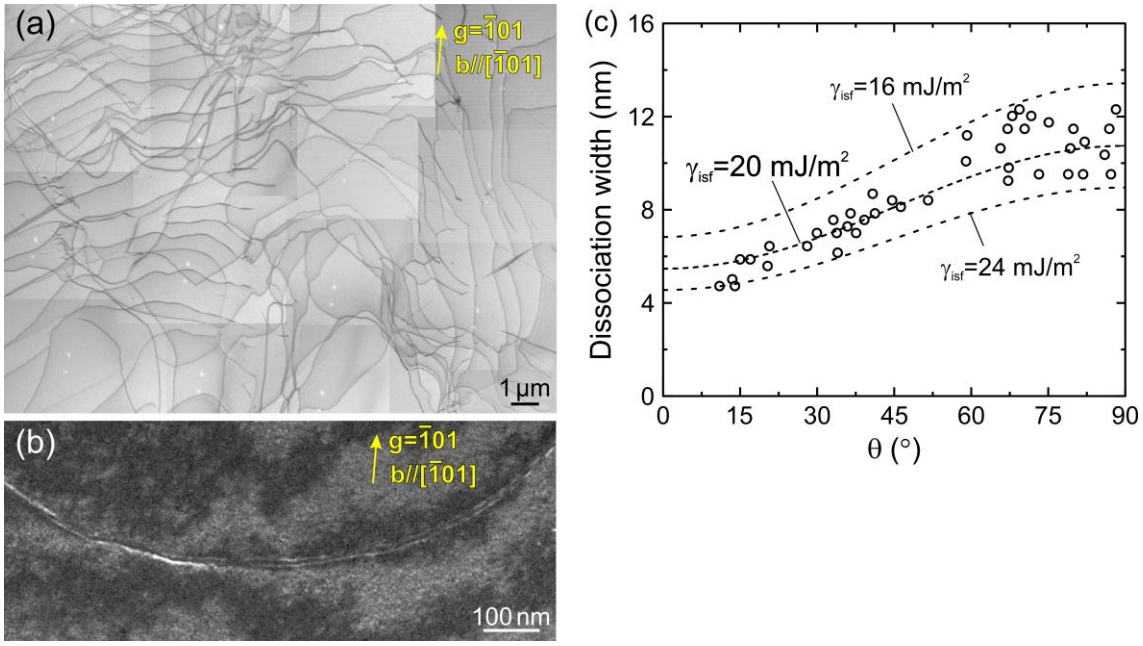

Fig. 3. (a) TEM bright-field and (b) weak-beam dark-field images of the equiatomic Cr-Fe-Co-Ni MEA deformed to about 2~3% plastic strain at room temperature. The thin foil was cut parallel to the (111) primary slip plane. (c) Dissociation widths of coupled Shockley partial dislocations plotted as a function of angle (θ) between the Burgers vector and dislocation line.

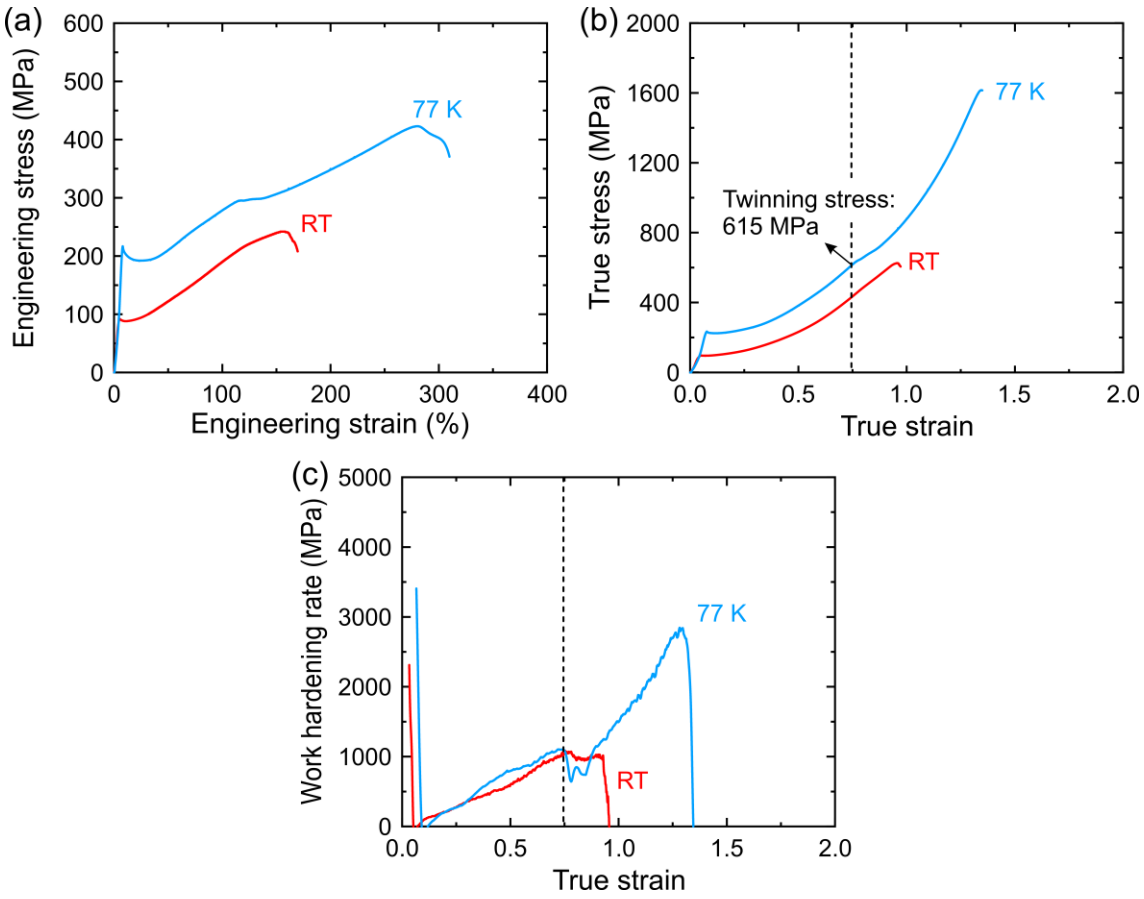

Fig. 4. (a) Engineering stress-strain and (b) true stress-strain curves for [$\bar{1}$23]-oriented single crystals of the equiatomic Cr-Fe-Co-Ni MEA deformed to failure in tension at 77 K and room temperature. (c) Work hardening rate for [$\bar{1}$23]-oriented single crystals of the equiatomic Cr-Fe-Co-Ni MEA calculated from (b) as a function of true strain.

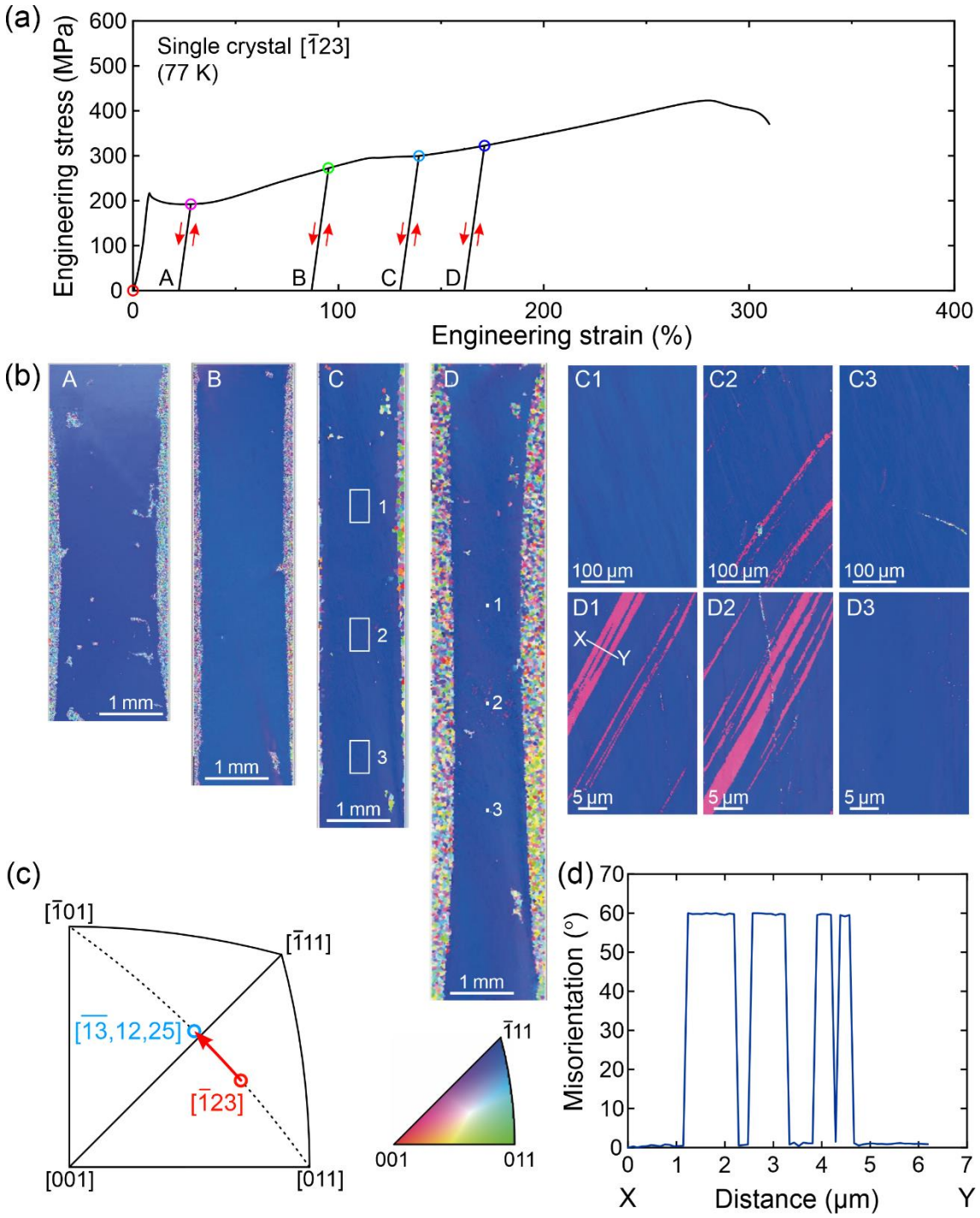

Fig. 5. (a) Tensile engineering stress-strain curve for a [$\bar{1}$23]-oriented single crystal of the equiatomic Cr-Fe-Co-Ni MEA deformed in tension at 77 K, in which the test was repeatedly interrupted at points A-D for microstructure observations. (b) EBSD orientation maps at the interruptions A-D with enlargements of the framed areas shown on the right-hand side for C-D. (c) Stereographic projection of the tensile-axis rotation during deformation. (d) Misorientation along the points X and Y in frame D1 in (b), showing the existence of deformation twins.

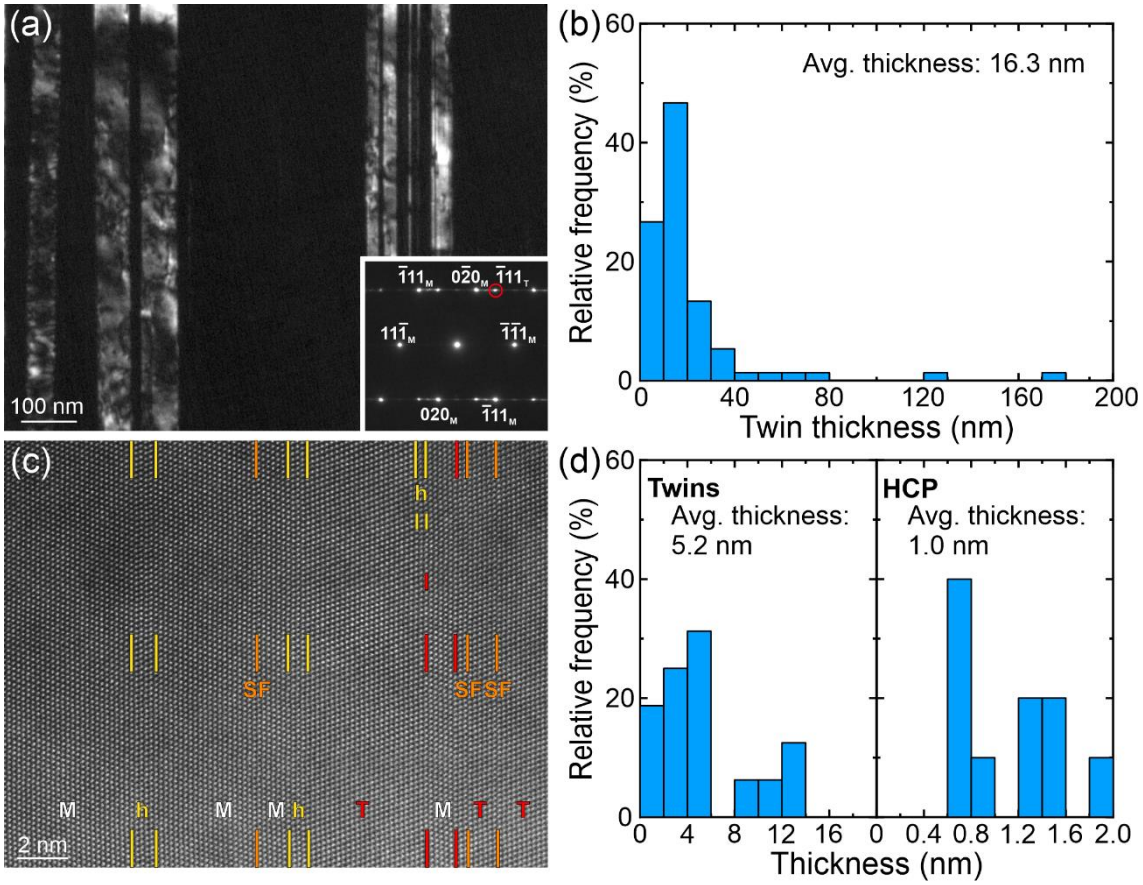

Fig. 6. (a) Typical dark-field TEM image of deformation twins in a $[\bar{1}23]$-oriented single crystal of the Cr-Fe-Co-Ni MEA deformed to failure at 77 K. The thin foil was cut perpendicular to the $(\bar{1}\bar{1}1)$ conjugate twinning planes. (b) Thickness distribution histogram of twins measured with dark-field TEM images. (c) Atomic-resolution STEM image of deformation twins in a $[\bar{1}23]$-oriented single crystal deformed to failure at 77 K. (d) Thickness distribution histograms of twins and HCP layers measured with atomic-resolution STEM images.

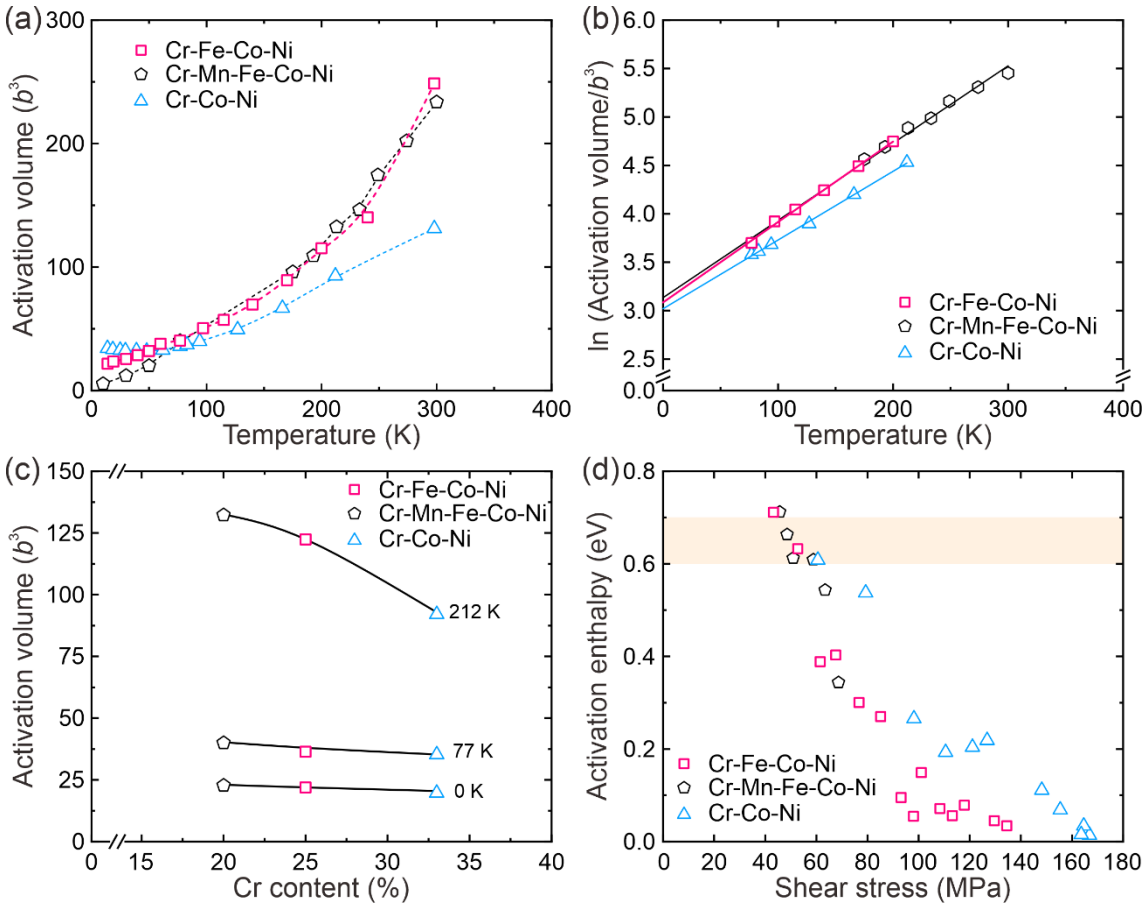

Fig. 7. (a) Temperature dependence of activation volume for deformation of single crystals of the three HEA/MEAs and (b) activation volumes of the three HEA/MEAs after fitting with equation (3). (c) Activation volumes plotted as a function of Cr content at selected temperatures. (d) The activation enthalpies for deformation estimated with the equation (4) plotted as a function of shear stress.

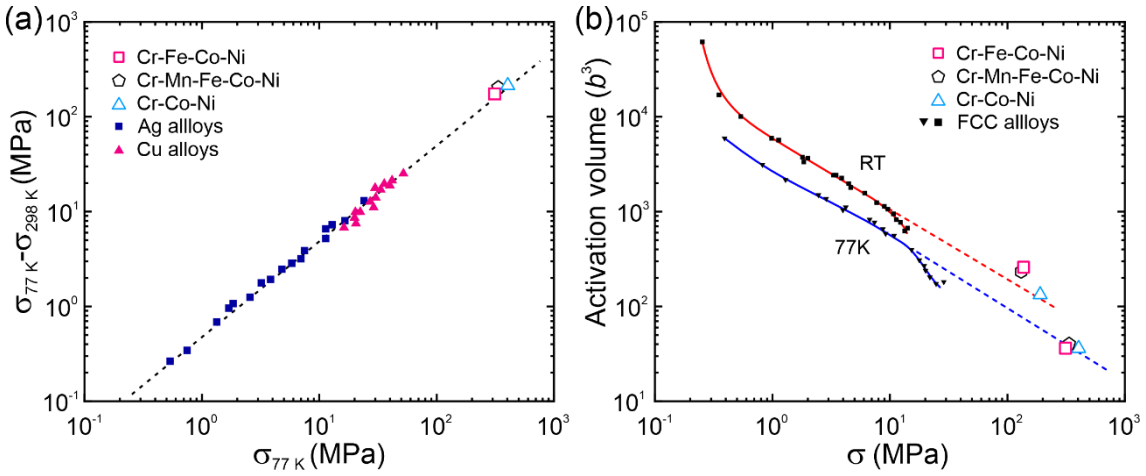

Fig. 8. (a) Difference between the yield stress at 77 K and that at room temperature plotted as a function of the yield stress at 77 K for FCC solid solutions and the three HEA/MEAs. (b) Activation volumes at 77 K and room temperature for FCC solid solutions and the three HEA/MEAs.

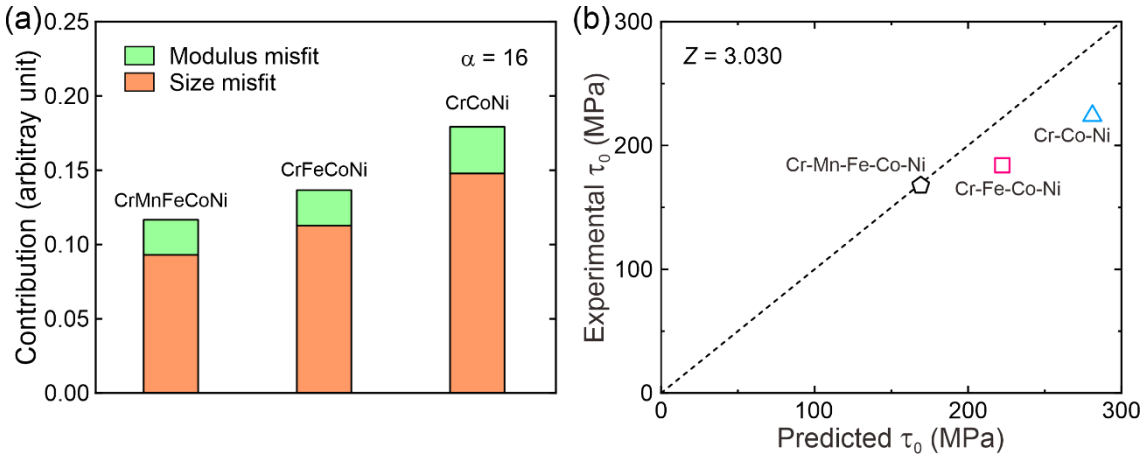

Fig. 9. (a) Contributions from the size misfit term and modulus misfit term to the 0 K CRSS estimated with equation (5) and (b) 0 K CRSS predicted with equation (6) and $Z = 3.030$ for the equiatomic Cr-Fe-Co-Ni MEA (this study), the equiatomic Cr-Mn-Fe-Co-Ni HEA (Kawamura et al., 2021) and the Cr-Co-Ni MEA (Li et al., 2022).

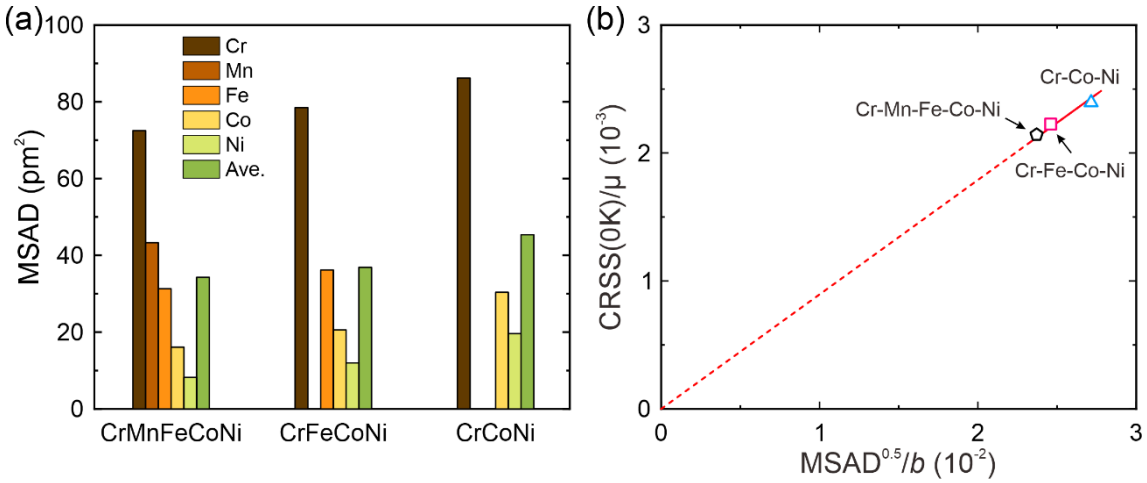

Fig. 10. (a) MSAD for each of the constituent elements and averaged values for the three alloys. (b) Relation between the experimental 0 K CRSS and MSAD for the three HEA/MEAs. The 0 K CRSS and MSAD are normalized by the shear modulus and dislocation Burgers vector, respectively.

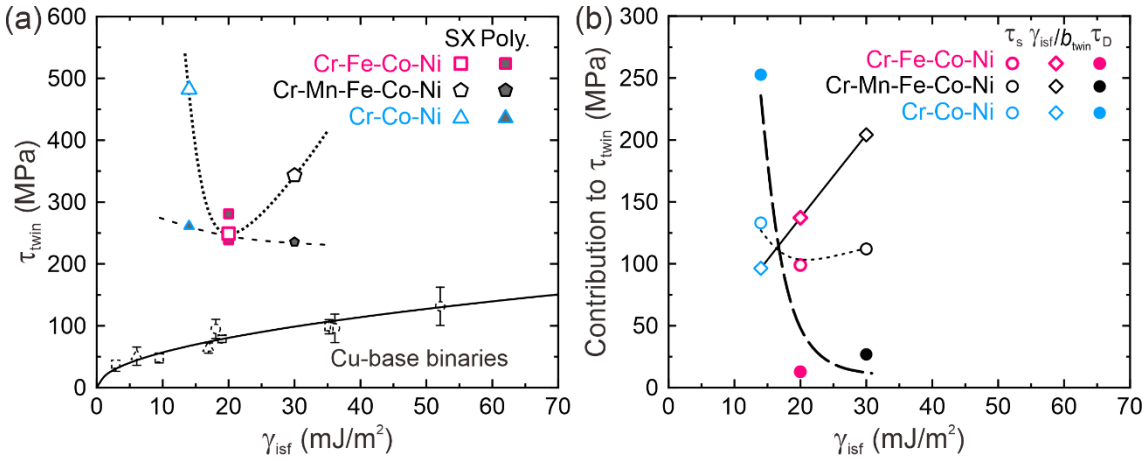

Fig. 11. (a) Relationship between the twinning shear stress at 77 K and stacking fault energy for [$\bar{1}$23]-oriented single crystals (solid symbols) and polycrystals (open symbols) of the equiatomic Cr-Mn-Fe-Co-Ni HEA and Cr-Fe-Co-Ni and Cr-Co-Ni MEAs, together with that reported previously for FCC slid-solution alloys. (b) The estimated contributions to the twinning shear stress from the three terms in equation (7) plotted as a function of stacking fault energy for the three HEA/MEAs.

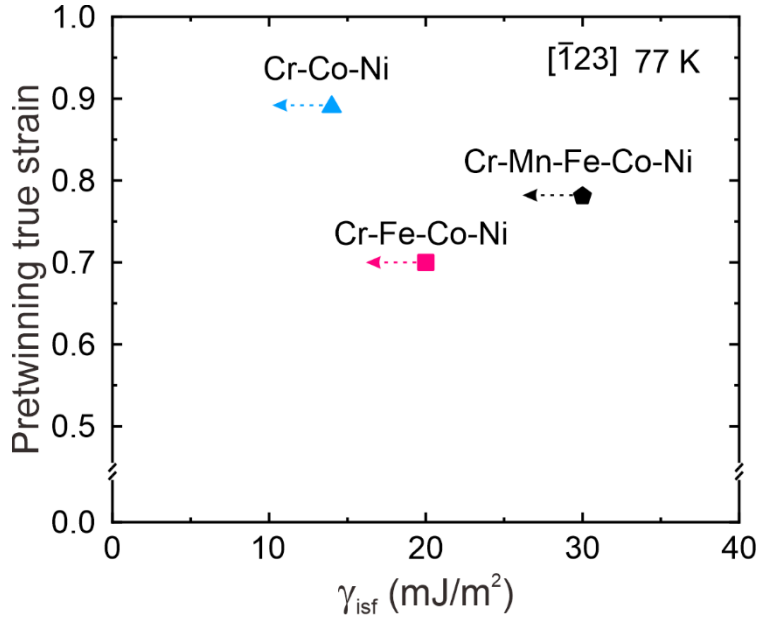

Fig. 12. True strain at the onset of deformation twinning at 77 K plotted as a function of stacking fault energy for the three HEA/MEAs.

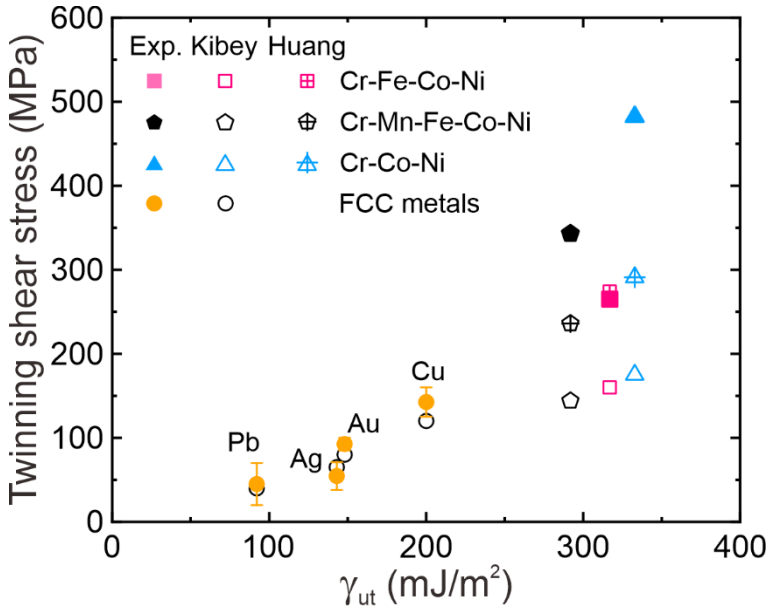

Fig. 13. Twinning shear stress of the three HEA/MEAs plotted as a function of unstable stacking fault energy calculated by Huang et al. (Huang et al., 2018): experimentally determined values for [$\bar{1}$ 23]-oriented single crystals (solid symbols), predicted values from models by Kibey et al. (Kibey et al., 2007a) (open symbols) and Huang et al. (Huang et al., 2018) (open with cross symbols). The data points for some pure FCC metals (Kibey et al., 2007a) are also shown for comparison.

Supplementary figures for

Plastic deformation of single crystals of the equiatomic Cr-Fe-Co-Ni medium entropy alloy – a comparison with Cr-Mn-Fe-Co-Ni and Cr-Co-Ni alloys to understand effects of Cr concentration

Le Li[1], Zhenghao Chen[1], Koretaka Yuge[1], Kyosuke Kishida[1], Haruyuki Inui[1], Martin Heilmaier[2], Easo P. George[3,4]

[1]Department of Materials Science and Engineering, Kyoto University, Sakyo-ku, Kyoto 606-8501, Japan
[2]Institute for Applied Materials (IAM-WK), Karlsruhe Institute of Technology (KIT), Engelbert-Arnold-Strasse 4, 76131 Karlsruhe, Germany
[3]Materials Science and Engineering Department, University of Tennessee, Knoxville, TN 37996, USA
[4]Institute for Materials, Ruhr University Bochum, 44801 Bochum, Germany

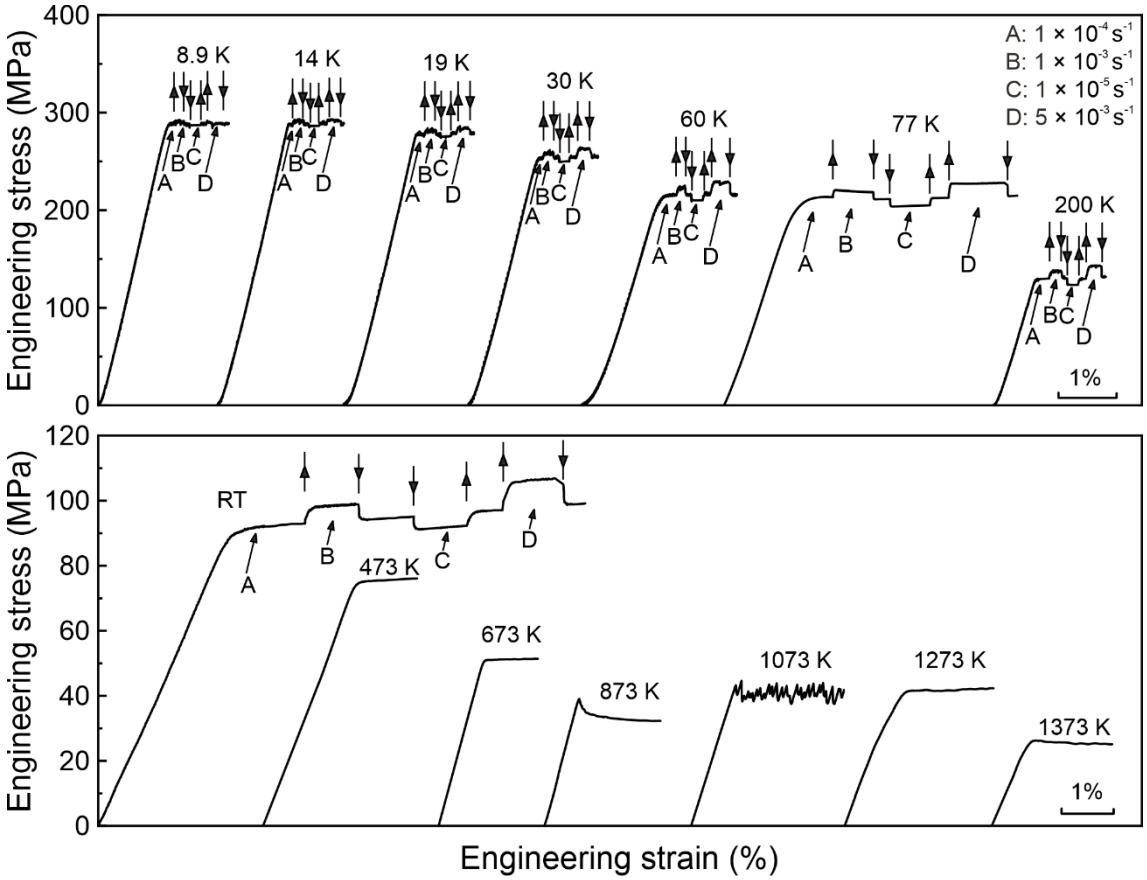

Fig. S1. Compressive stress-strain curves at selected temperatures for [$\bar{1}$23]-oriented single crystals of the equiatomic Cr-Fe-Co-Ni MEA. Compression tests were usually started at a strain rate of 1×10^{-4} s^{-1} to determine the yield stress and then strain-rate sensitivity was measured by strain-rate jump tests as indicated with arrows (at room temperature and below).

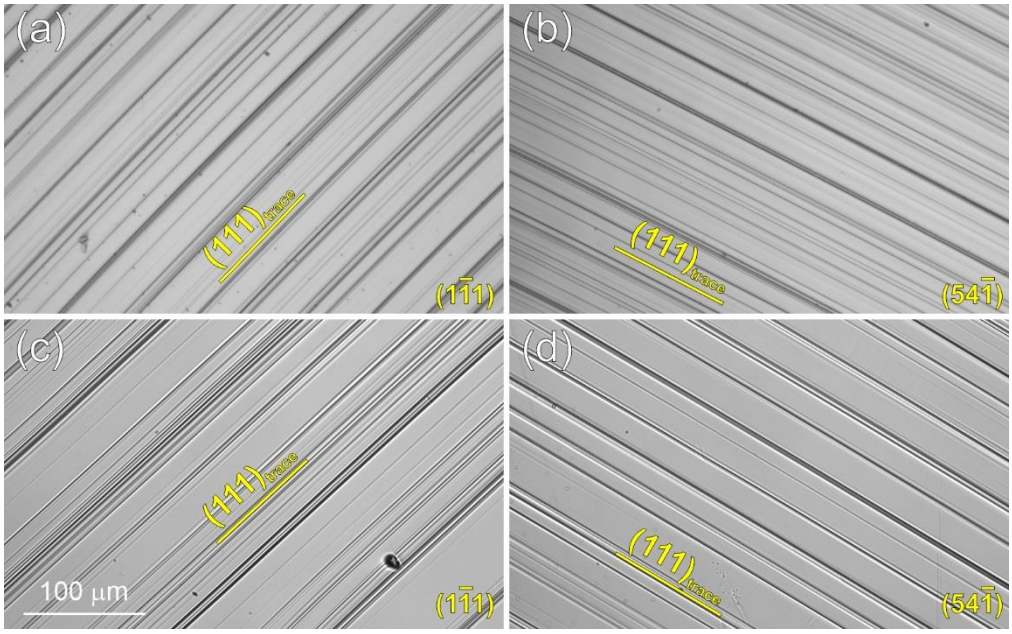

Fig. S2. Deformation markings observed on two orthogonal side surfaces ((a,c) $(1\,\bar{1}\,1)$ and (b,d) $(54\,\bar{1})$) of $[\bar{1}\,23]$-oriented single crystals deformed in compression at (a,b) 77 K and (c, d) room temperature.

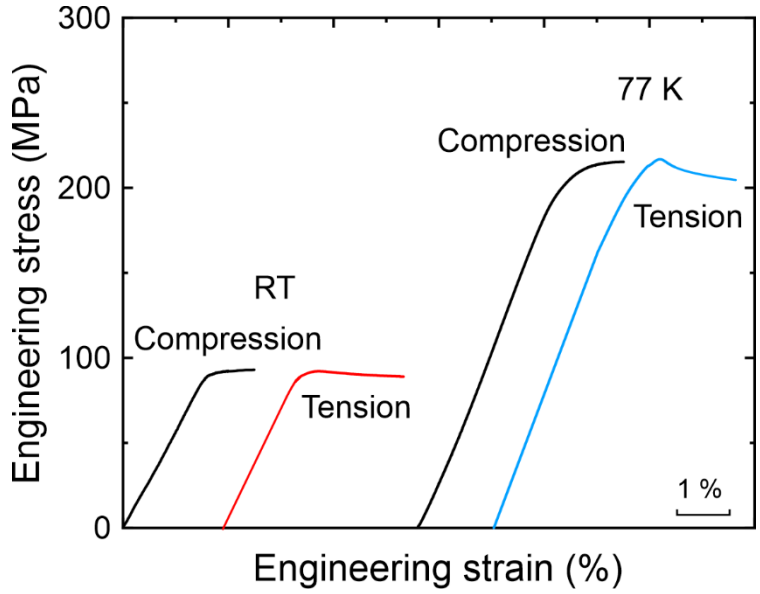

Fig. S3. Tensile and compressive stress-strain curves at 77 K and room temperature for $[\bar{1}\,23]$-oriented single crystals of the equiatomic Cr-Fe-Co-Ni MEA.

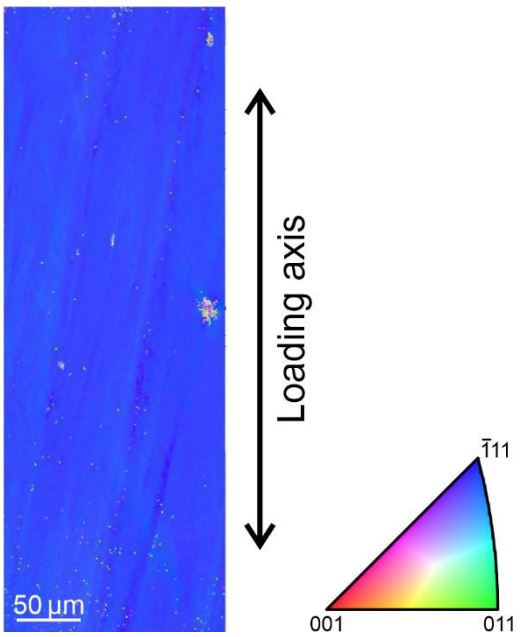

Fig. S4. EBSD orientation map of a [$\bar{1}$23]-oriented single crystal of the equiatomic Cr-Fe-Co-Ni MEA deformed in tension to failure at room temperature. There is no indication that deformation twinning occurred.

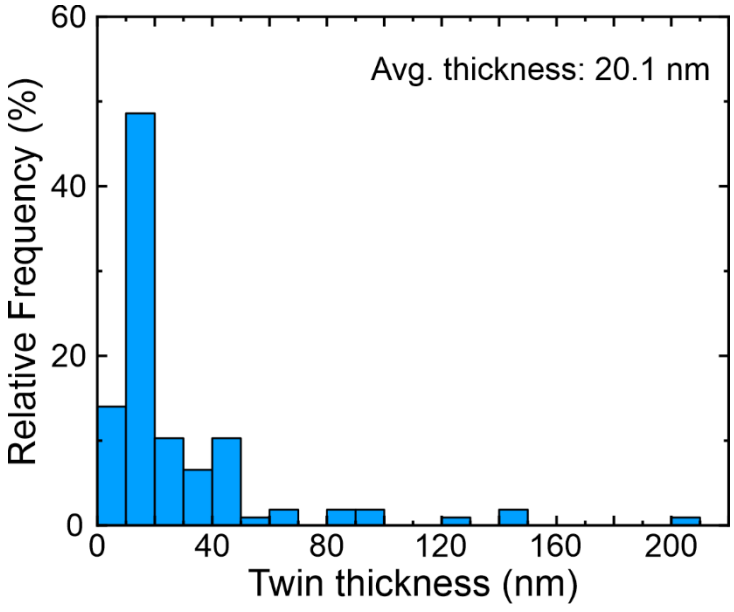

Fig. S5. Twin thickness distribution in [$\bar{1}$23]-oriented single crystals of the equiatomic Cr-Mn-Fe-Co-Ni HEA deformed in tension to failure at 77 K measure from dark-field TEM images (Kawamura et al., 2021).

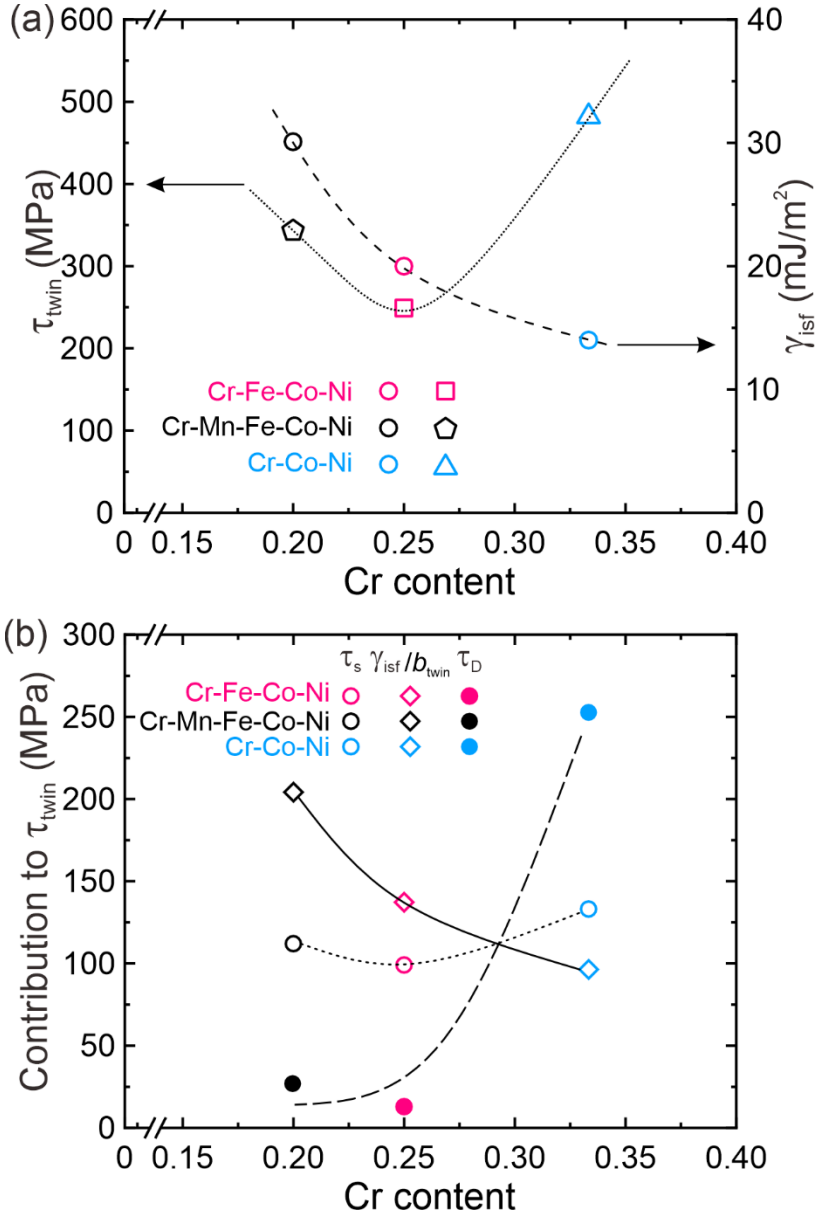

Fig. S6. (a) The stacking fault energy (right Y axis) and the twinning shear stress at 77 K (left Y axis) plotted as against Cr content for [$\bar{1}$23]-oriented single crystals of the equiatomic Cr-Mn-Fe-Co-Ni HEA and Cr-Fe-Co-Ni and Cr-Co-Ni MEAs. (b) The estimated contributions to the twinning shear stress from the three terms in equation (7) plotted as a function of Cr content for the three HEA/MEAs.